Electronic Supplementary Information

Nanoconfined tandem three-phase photocatalysis for highly selective CO_2 reduction to ethanol

Hailing Huo, [a] Ting Hu, [a] Zhiqing Zhong, [a] Cheng Zhan, [a] Chengxi Huang, [a] Qiang Ju, [a] Liang Zhang, [a] Fang Wu, [b] Erjun Kan,*[a] and Ang Li*[a]

a H. Huo, Dr. T. Hu, Z. Zhong, Prof. C. Zhan, Prof. C. Huang, Q. Ju, L. Zhang, Prof. E. Kan, Prof. A. Li
MIIT Key Laboratory of Semiconductor Microstructure and Quantum Sensing, School of Science
Engineering Research Center of Semiconductor Device Optoelectronic Hybrid Integration in Jiangsu Province
Nanjing University of Science and Technology
Nanjing 210094, P. R. China
E-mail: liang2100@njust.edu.cn
ekan@njust.edu.cn

b Prof. F. Wu
College of Information Science and Technology
Nanjing Forestry University
Nanjing 210037, P. R. China.

Experimental Procedures

Chemicals

Copper nitrate ($Cu(NO_3)_2 \cdot 3H_2O$, AR) and potassium bicarbonate ($KHCO_3$, AR) were purchased from Macklin. Ascorbic acid (AR) and 1-dodecanethiol ($C_{12}H_{25}$-SH, 99.5%) were purchased from Aladdin. Sodium hydroxide (NaOH, AR), methanol (AR), ethanol (AR), silver nitrate ($AgNO_3$, >99.0%), and ammonium sulfate ($(NH_4)_2SO_4$, AR) were purchased from Sinopharm Chemical Reagent Co., Ltd. Polyvinylpyrrolidone (PVP, M.W = 30000) was purchased from Shanghai Yuanye Bio-Technology Co., Ltd. Sodium chloride (NaCl) was purchased from China National Medicines Corporation Ltd. Nafion® D520 dispersion was purchased from 3AMaterials®. Deionized water (DI water, 18.25 MΩ·cm) obtained from a UP Water Purification System was used throughout the experimental processes. All chemicals were obtained from commercial suppliers and used without further purification.

Sample preparation

Synthesis of quasi-spherical silver (Ag) particles. Following the synthesis method documented in the literature with some modifications, silver chloride (AgCl) colloid was initially synthesized, serving as a precursor for the subsequent synthesis of monodispersed Ag particles. Specifically, 127.5 mg of PVP was dissolved in 30 mL of DI water, followed by the addition of 127.5 mg of $AgNO_3$. Upon complete dissolution, 300 μL of 5 M NaCl solution was added and the mixture was stirred in darkness for 15 min to form an AgCl colloid. Subsequently, 25 mL of the synthesized AgCl colloid was combined with 200 mL of 50 mM ascorbic acid solution, and then 26 mL of 0.5 M NaOH solution was added. The mixture was stirred in darkness at room temperature for 2 h. The resulting product was collected through centrifugation and washed with DI water.

Synthesis of Ag@Cu_2O sphere. 2.4 mg of Ag particles was dispersed in 400 mL of 2 mM PVP solution. After vigorous stirring for 10 min, 228.8 mg of $Cu(NO_3)_2 \cdot 3H_2O$ was added, followed by 462.4 mg of $(NH_4)_2SO_4$. After stirring for 5 min, 16 mL of 0.2 M NaOH solution was injected dropwise, with continued stirring for 2 min. Subsequently, 28 mL of 0.1 M ascorbic acid solution was added dropwise, and stirring was maintained for 13 min. The resulting product (Ag@Cu_2O) was collected through centrifugation, washed with DI water and ethanol several times, and finally dried in a vacuum oven. To further explore the impact of different synthesis scales on the sample, the synthesis process was adjusted to include scales of 100 mL, 800 mL, and 1200 mL, in addition to the original 400 mL scale. The quantities of reagents were proportionally adjusted for each scale. For example, the reagent amounts were reduced to one-quarter for the 100 mL scale and doubled for the 800 mL scale. Apart from the changes in scale and reagent quantities, all other operating conditions, such as reagent concentration, stirring time, and reaction time, were kept consistent throughout the synthesis process.

Synthesis of bare Cu_2O sphere (b-Cu_2O). To compare the impact of Ag particles on catalyst performance, bare Cu_2O (b-Cu_2O) was synthesized as a control sample. The synthetic process of b-Cu_2O was similar to that of Ag@Cu_2O, with the exception that the addition of Ag particles was unnecessary.

Synthesis of Ag/Cu_2O. To investigate the impact of the spatial position of Ag particles on catalyst performance, a structure in which Ag particles were loaded outside Cu_2O spheres was synthesized as a control sample. The external loading of Ag particles onto Cu_2O was achieved using a photodeposition technique. Specifically, 50 mg of the synthesized b-Cu_2O was dispersed in 50 mL of DI water by ultrasound, followed by the addition of 15 mL of methanol as a hole sacrificial agent, and then 0.6 mL of 0.025 M $AgNO_3$ solution was added. The photodeposition process occurred

under visible light in a vacuum environment, with a deposition time of 3 h. A 300 W Xe lamp with a 420 nm filter served as the light source. The resulting product was collected through centrifugation, washed with DI water and ethanol several times, and finally dried in a vacuum oven.

Surface modification to synthesize hydrophobic structures. The as-prepared samples of Ag@Cu_2O, Ag/Cu_2O, and b-Cu_2O were all treated with 1-dodecanethiol (DDT) to modify their wettability to be hydrophobic. The resulting hydrophobic samples were denoted as O-Ag@Cu_2O, O-Ag/Cu_2O, and O-b-Cu_2O, respectively. In a typical procedure, 10 mg of Cu_2O was ultrasonically dispersed in 10 mL of ethanol, followed by the injection of 7 μL of DDT. The mixture was then gently stirred at room temperature for 40 min. The resultant product was collected through centrifugation, followed by repeated washing with ethanol, and finally dried in a vacuum oven. Furthermore, samples synthesized at different scales (100 mL, 800 mL, and 1200 mL) during the Ag@Cu_2O process underwent the same hydrophobic treatment. This was carried out to assess the influence of synthesis scale on the final catalyst, O-Ag@Cu_2O.

Characterizations

Transmission electron microscopy (TEM) was performed using a JEOL JEM 2100F electron microscope. Crystalline structures were evaluated by X-ray diffraction (XRD) analysis using a Bruker D8 Focus operating at 40 kV and 40 mA, equipped with nickel-filtered Cu Kα radiation (λ = 1.54056 Å). Specific surface areas and pore structures of catalysts were measured using Micromeritics ASAP 2460 through nitrogen adsorption at 77 K. The specific surface areas were calculated from the isotherms using the BET method. The pore distribution was obtained by the BJH method from the adsorption branch of the adsorption isotherms. Room temperature steady-state photoluminescence (PL) spectra were performed on an FL 970 fluorescence spectrophotometer under an excitation wavelength of 405 nm. UV-vis diffuse reflectance spectra were recorded using UV-2600 under the visible light of 400 - 800 nm. Reflectivity was used to measure light absorption through the conversion of the Kubelka-Munk formula, and $BaSO_4$ was used as the reference sample. X-ray photoelectron spectroscopy (XPS) was performed on Thermo Fischer ESCALAB 250Xi with an Al K X-ray source to reveal chemical states, and the binding energies (BE) were calibrated using the C 1s electron peak (BE = 284.8 eV). Raman spectra were recorded using the Raman spectrometer DXR2. In situ Fourier transform infrared spectroscopy (FTIR) spectra were performed on the Thermo Fisher Nicolet IS50. Water contact angles were measured using an SDC-350 instrument, with the samples uniformly dispersed on glass substrates using ethanol as a solvent. The volume of the water droplet was 7 μL, and the final results were average values obtained from more than three positions.

Supplementary tests

K^+ tracing experiment. To investigate whether the presence of DDT in mesoporous channels would hinder water from entering the mesoporous channels, a potassium ion (K^+) tracing experiment was conducted to directly observe the entry position of water into the mesoporous channels by studying K^+ distribution. Specifically, 10 mg of O-Ag@Cu_2O was dispersed in 10 mL of 0.2 M $KHCO_3$ solution, followed by gentle stirring for 10 min. Subsequently, the sample was centrifuged and washed once with DI water. The resultant sample was dropped onto a molybdenum mesh for TEM testing, EDS mapping and line scanning observations.

Ag^+ probe experiment. Ag^+ probe experiments were conducted to confirm that the hydrophobic treatment did not hinder the migration of charge carriers to the catalyst surface. Ag^+ (derived from $AgNO_3$) and methanol were used as the probe ion and hole charge scavenger, respectively. Typically, 15 mg of catalysts (O-Ag@Cu_2O or Ag@Cu_2O) were dispersed in 30 mL of DI water. Then 15 mL of methanol and 1.2 mL of $AgNO_3$ solution (0.025 M) were added. After stirring and

evacuation for 0.5 h, the mixture was irradiated with a 300 W Xe lamp (λ > 420 nm) for 3 h. The Ag-loaded catalyst was obtained after centrifugation, washing, and drying procedures. During the experiment, Ag^+ would be reduced to Ag particles by the photogenerated electrons migrating to the catalyst surface. Therefore, by comparing the amount of deposited Ag on O-Ag@Cu_2O and Ag@Cu_2O, the amount of photogenerated electrons transferred to the catalyst surface can be compared.

Photocurrent measurement. Photoelectrochemical measurements were conducted using a CHI-660E electrochemical workstation from China. The measurements were performed in a standard three-electrode configuration, with the prepared samples serving as the working electrode, a platinum plate as the counter electrode, and the standard Ag/AgCl electrode as the reference. A 0.2 M Na_2SO_4 aqueous solution was used as the electrolyte. The working electrode was prepared as follows: 8 mg of catalyst was dispersed in 2 mL of H_2O, 2 mL of isopropanol, and 190 μL of Nafion® D520 dispersion. Then 100 μL of the aforementioned mixture was dropped onto an FTO glass with an area of 1 cm^2. The photocurrent of the samples was measured under a 300 W Xe lamp (PLS-SXE300, PerfectLight, China) irradiation equipped with a 420 nm cutoff filter. The light on/off cycle was set to 10 s.

CO_2 photoreduction test. The performance of catalysts for PCRR was evaluated using Labsolar 6A (PerfectLight, China) and gas chromatography (GC, Agilent 8890, America).

Before illumination, 30 mg of catalysts was added to 100 mL of $KHCO_3$ (0.1 M) aqueous solution without using hole scavengers. The mixture was magnetically stirred in a double-layer Pyrex glass reactor (PerfectLight, China). The reactor was then connected to Labsolar 6A and evacuated. Subsequently, compressed CO_2 (99.999%) was bubbled into the reactor to raise the system pressure to 80 kPa. The system was then evacuated again. This extraction-inflation operation was repeated three times to remove as much air as possible. Finally, pure CO_2 was continuously bubbled through the solution again to raise the CO_2 pressure to 80 kPa. Then the system was maintained for 40 min to reach CO_2 dissolution equilibrium. A 300 W Xe lamp (PLS-SXE300, PerfectLight, China) with a cutoff 420 filter was then used as the light source through the quartz window. The distance between the light source and the quartz window was kept constant at 10 cm. During the reaction, 1.5 mL of liquid products was taken out using a syringe every hour for subsequent analysis. Comparative experiments were carried out under similar experimental conditions.

The amounts of gaseous and liquid products that evolved were all determined using GC. Gas products were directly detected by GC, which was equipped with a thermal conductivity detector (TCD), a flame ionization detector (FID), and a methanation reactor. For liquid products, the samples obtained at each hour were injected into GC through a headspace sampler (APL HS-20, China) for analysis. Specifically, 200 μL of the extracted liquid was mixed with 5 mL of H_2O in each headspace bottle, and then the bottle was placed into the headspace sampler. The liquid products were automatically injected into the GC for detection. An external standard was used to calculate the amount of each component based on the peak area of GC.

Careful calculation is required to determine the amount of O_2. The presence of a potential air leak during the reaction introduces the possibility of O_2 from the ambient air entering the reaction system, leading to inaccuracies in determining the generated O_2 content. To mitigate this error, calibration was performed by comparing the O_2 content generated from the reaction with the N_2 content, allowing for the accurate determination of the actual amount of generated O_2. Specifically, as N_2 cannot be generated from the OPCRR, the detection of N_2 in the GC signifies its origin as air leakage. Considering a volume ratio of 20.9: 78.1 for O_2 to N_2 in ambient air, the quantity (mL) of O_2 resulting from air leakage can be determined based on the corresponding volume (mL) of N_2. Consequently, the volume (mL) of O_2 generated by the reaction can be obtained by subtracting the volume (mL) of O_2 caused by air leakage.

Isotope-labeling test. The isotope labeling experiment was conducted as follows. Firstly, 30 mg of O-Ag@Cu_2O was added to 50 mL of $NaH^{13}CO_3$ (0.1 M) solution in the reactor for ultrasonic dispersion. Subsequently, the reactor was connected to Labsolar 6A, sealed, and purged with flowing Ar for 60 min to remove air. Afterwards, $^{13}CO_2$ (99.999%) was introduced into the reactor, raising the final pressure for the reaction to 80 kPa. The reactor was allowed to stabilize for 40 min, after which the PCRR was performed for 4 h using a 300 W Xe lamp with a cutoff 420 filter. The products containing C-isotopes were analyzed by gas chromatography-mass spectrometry (GC-MS) (Shimadzu QP-2010SE).

Calculation of selectivity. The selectivity from the PCRR on an electron basis ($6e^-$ for CH_3OH, $12e^-$ for CH_3CH_2OH, $2e^-$ for H_2) was calculated using equation (1):

$$\text{Selectivity of ethanol (\%)} = 12\, n_{\text{ethanol}} \times 100\% / (6\, n_{\text{methanol}} + 12\, n_{\text{ethanol}} + 2\, n_{\text{hydrogen}}) \quad (1)$$

where n_{methanol}, n_{ethanol}, and n_{hydrogen} represent the amounts (moles) of methanol, ethanol, and hydrogen formed within a certain period, respectively.

Calculation of solar-to-fuel conversion efficiency. The solar-to-fuel conversion efficiency (STF) can be quantified as the ratio of the chemical energy output for the production of fuels to the solar energy input. It can be calculated using equation (2):[1]

$$\text{STF (\%)} = \text{Output energy for fuels evolved} \times 100\% / \text{Energy of incident solar light} \quad (2)$$

This equation can be further expanded as:

$$\text{STF (\%)} = [R_{\text{methanol}}\ (\mu\text{mol h}^{-1}) \times \Delta G_{\text{r(methanol)}}\ (\text{kJ mol}^{-1}) + R_{\text{ethanol}}\ (\mu\text{mol h}^{-1}) \times \Delta G_{\text{r(ethanol)}}\ (\text{kJ mol}^{-1})] \times 100\% / P\ (\text{mW cm}^2) \times S\ (\text{cm}^2)$$

where R_{methanol} and R_{ethanol} indicate the rate of methanol and ethanol formation during the PCRR, respectively. $\Delta G_{\text{r(methanol)}}$ and $\Delta G_{\text{r(ethanol)}}$ represent the Gibbs energy change for the CO_2-to-CH_3OH and CO_2-to-CH_3CH_2OH reactions, respectively. P is the average irradiation intensity, and S is the incident irradiation area. For this study, S is determined to be 19.625 cm^2.

The irradiation intensity of the 300 W Xe lamp with a 420 nm filter was measured using a CEL-FZ-A Optical Power Meter. Five different test positions (Fig. S21a) were adopted to determine the average irradiation intensity P, and it was found to be 125.58 mW cm^{-2} (Fig. S21b), following equation (3).[2]

$$P = P_{\text{center}} / 3 + 2P_{\text{edge}} / 3 \quad (3)$$

The reaction Gibbs energy change ΔGr can be calculated using equation (4):

$$\Delta G_r = \sum \nu_i \Delta_f G_i \quad (4)$$

where ν_i is the stoichiometric coefficient for species i in the formation reaction. $\Delta_f G_i$ is the molar Gibbs energy of formation for species i. In this study, the PCRR conditions are approximated as standard states, and the thermodynamic data used are summarized in Table S3.[3]

Considering the CO_2-to-CH_3OH reaction with the chemical formula: $CO_2 + 2H_2O \rightarrow CH_3OH + 3/2O_2$. Thus, $\Delta G_{\text{r(methanol)}}$ can be calculated as follows:

$$\Delta G_r = \Delta_f G_{\text{methanol}}^{\Theta} + 3/2\Delta_f G_{\text{oxygen}}^{\Theta} - \Delta_f G_{\text{carbon dioxide}}^{\Theta} - 2\Delta_f G_{\text{water}}^{\Theta}$$

$$= (-166.3)\ \text{kJ mol}^{-1} - (-394.4)\ \text{kJ mol}^{-1} - 2 \times (-237.1)\ \text{kJ mol}^{-1} = 702.3\ \text{kJ mol}^{-1}$$

CO_2-to-CH_3CH_2OH reaction with the chemical formula: $2CO_2 + 3H_2O \rightarrow CH_3CH_2OH + 3O_2$. Thus, $\Delta G_{\text{r(ethanol)}}$ can be calculated as follows:

$$\Delta G_r = \Delta_f G_{\text{ethanol}}^{\Theta} + 3\Delta_f G_{\text{oxygen}}^{\Theta} - 2\Delta_f G_{\text{carbon dioxide}}^{\Theta} - 3\Delta_f G_{\text{water}}^{\Theta}$$

$$= (-174.8)\ \text{kJ mol}^{-1} - 2 \times (-394.4)\ \text{kJ mol}^{-1} - 3 \times (-237.1)\ \text{kJ mol}^{-1} = 1325.3\ \text{kJ mol}^{-1}$$

Combining the values of $R_{methanol}$ (55.95 μmol g^{-1} h^{-1} × 0.03 g = 1.679 μmol h^{-1}) and $R_{ethanol}$ (450.19 μmol g^{-1} h^{-1} × 0.03 g = 13.506 μmol h^{-1}), the STF was calculated to be 0.215%.

Calculation of apparent quantum efficiency (AQE). The photocatalytic activity of the target catalyst at a specific excitation wavelength was obtained by a specific bandpass filter with a 300 W Xe lamp in the same apparatus as the CO_2 photoreduction performance test. Generally, AQE is calculated using equation (5):

AQE (%) = Number of electrons involved in the reaction × 100% / Number of incident photons (5)

Thus, for the photocatalytic reduction of CO_2 to fuels, AQE is calculated by the following equation:

$$AQE\ (\%) = [6n_{methanol} + 12n_{ethanol}] \times N_A \times 100\% / N_P \quad (6)$$

where $n_{methanol}$ and $n_{ethanol}$ are the amounts (moles) of CH_3OH and CH_3CH_2OH formed within 1 h, respectively. N_A is the Avogadro constant (6.02×10^{23} mol^{-1}), and N_P is the number of incident photons. In the actual measurement, it is assumed that all incident photons are absorbed by the suspension and the calculation formula of N_P is the following equation (7):

$$N_P = PSt\lambda / hc \quad (7)$$

where P is the average intensity of the radiation and five different test positions are adopted to determine it (Fig. S21c), S is the incident irradiation area (S = 19.625 cm^2), t is the irradiation time (t = 1×3600 s), λ is the incident wavelength, h is the Planck constant (6.626×10^{-34} J s), and c is the speed of light (3×10^8 m s^{-1}).

In situ Fourier-transform infrared spectroscopy (FTIR) test. Diffuse reflection in situ FTIR was used to investigate effective CO_2 adsorption on the catalyst surface and detect possible intermediates during the overall PCRR. 50 mg of the catalyst was loaded onto the sample cell of the diffuse reflectance attachment, ensuring a flat top surface. A cover was fixed on the sample holder to form a reaction space, which was then cleaned by Ar. Then the FTIR data was collected as the background. Subsequently, visible light was introduced into the reaction space through the observation window, and CO_2 was introduced via a container. It should be noted that the container was filled with water to ensure the formation of a water film on the sample powders. FTIR data was collected every 10 min to monitor and record any changes.

Computational details.

All optimized geometries and electronic energies based on the spin-polarized density functional theory (DFT) were performed using the Vienna *ab initio* simulation package.[4, 5] The exchange-correlation function was treated within the generalized gradient approximation (GGA) and parameterized by the Perdew-Burke-Ernzerhof (PBE) formula to describe the electronic exchange and correlation effects. Van der Waals interactions were described using the empirical correction in Grimme's scheme (DFT-D3). The plane wave cutoff energy was 500 eV. The geometry structure optimization was performed using the conjugated gradient minimization scheme with the atomic positions fully relaxed. The convergence criteria for electronic and ionic relaxations are 10^{-5} eV/atom and 0.05 eV/Å, respectively. The vacuum space was set to be more than 20 Å, which was large enough to avoid interactions between periodic layers. The dipole correction was also included in calculations to eliminate spurious electrostatic interaction between periodic copies in the z direction. The 2D Brillouin integration was sampled with a 3×3×1 Monkhorst–Pack grid. The free energy difference of each elemental reaction step is calculated as $\Delta G = \Delta E + \Delta E_{ZPE} - T\Delta S$, where ΔE is the electronic energy difference directly obtained from DFT calculations, ΔE_{ZPE} is the change in zero-point energies, T is the temperature, which is set to be 300 K; ΔS is the entropy change. The E_{ZPE} and TS for each reaction intermediates can be calculated by the following equations, respectively:

$$E_{ZPE} = \frac{1}{2} \sum_i h\nu_i$$

$$-TS=k_{\mathrm{B}}\mathrm{T}\sum_{\mathrm{i}}\ln\left(1-\mathrm{e}^{-\frac{h\nu_i}{k_BT}}\right)-\sum_{\mathrm{i}}h\nu_{\mathrm{i}}\left(\frac{1}{\mathrm{e}^{\frac{h\nu_i}{k_BT}}-1}\right)$$

where h, ν, and k_{B} are Planck constant, vibrational frequencies and Boltzmann constant, respectively.

The Cu_2O (111) surface was constructed, and a 3×3 supercell with three layers was selected as the computational model. The Cu_2O catalyst in contact with Ag particles was modeled with a 4-atom Ag cluster on the Cu_2O (111) surface (made of a layer of three atoms in contact with Cu and one Ag atom on top of it).

Results and Discussion

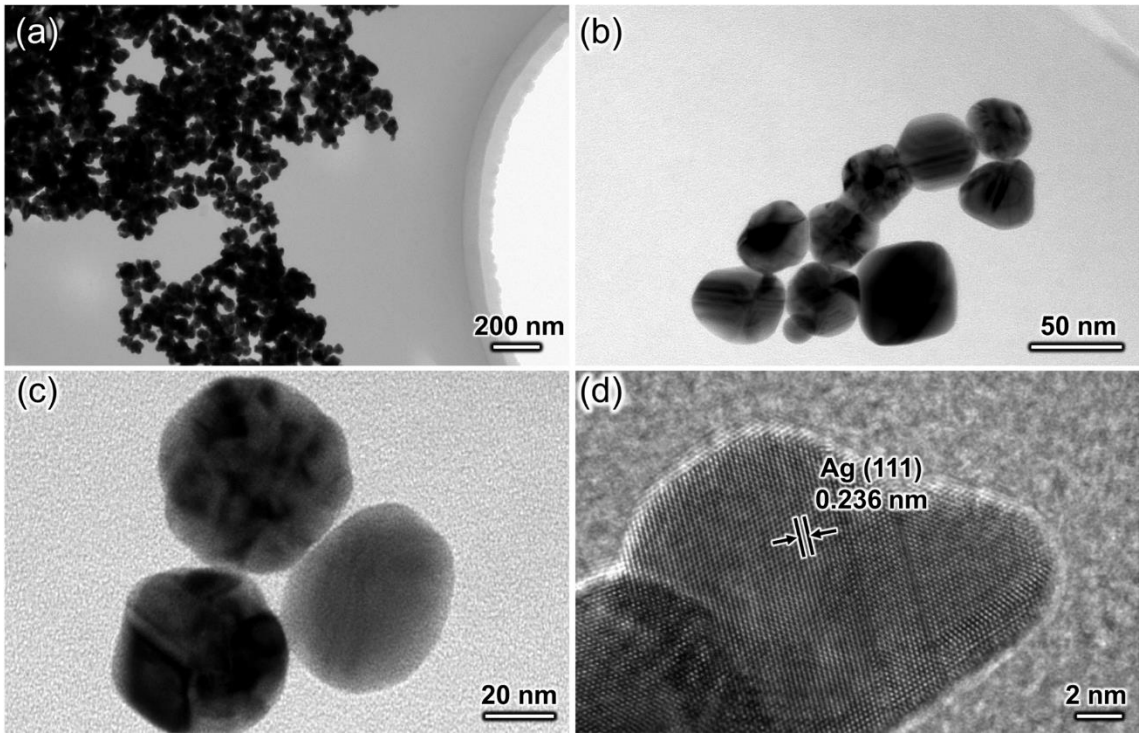

Fig. S1. Morphology of Ag particles. (a-c) TEM images. (d) HRTEM image. The Ag particles exhibit a uniform quasi-spherical shape with an approximate size of 40 nm. The lattice spacing of 0.236 nm depicted in Fig. S1d is consistent with the (111) planes of Ag, indicating the successful synthesis of Ag particles.

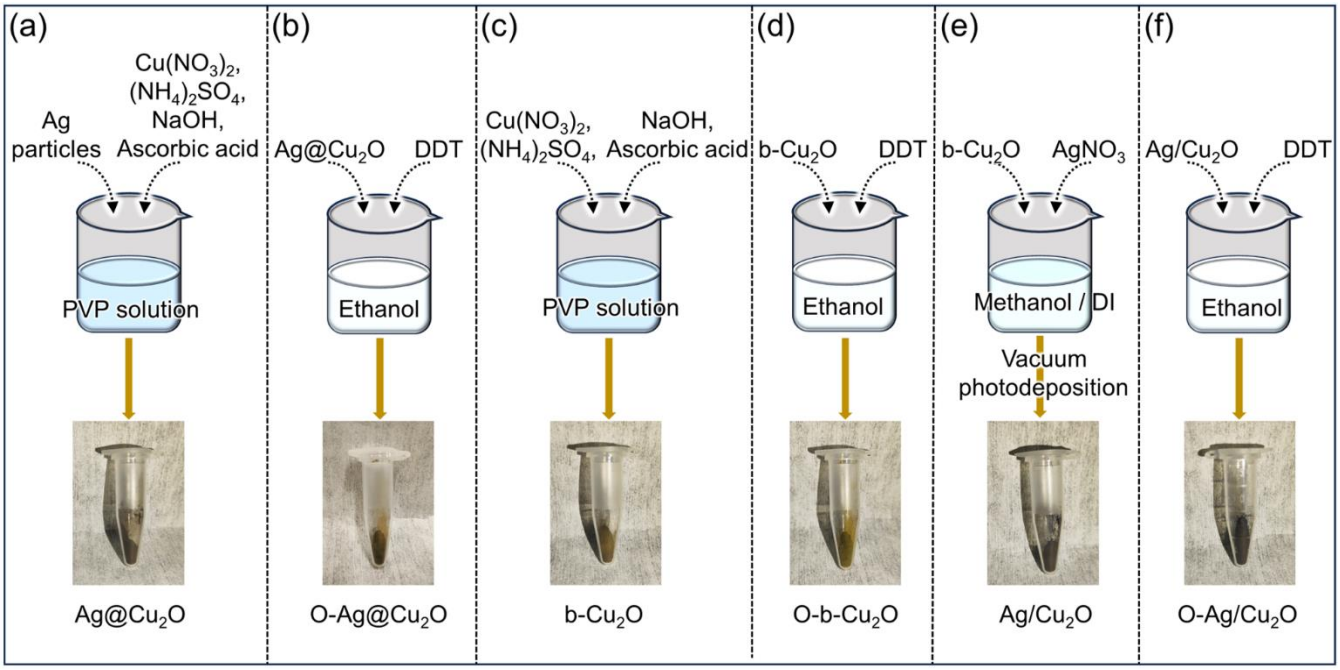

Fig. S2. Preparation processes and photographs for different samples. (a) Ag@Cu_2O. (b) O-Ag@Cu_2O. (c) b-Cu_2O. (d) O-b-Cu_2O. (e) Ag/Cu_2O. (f) O-Ag/Cu_2O.

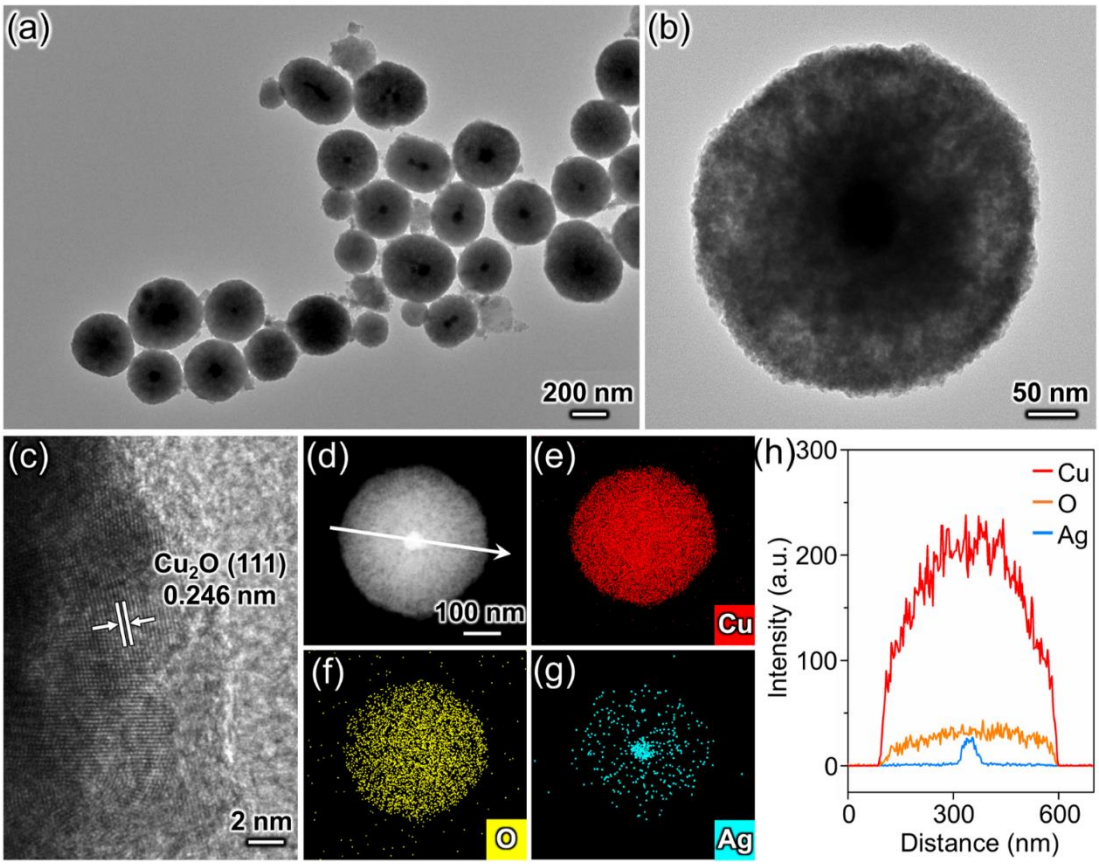

Fig. S3. Morphology of Ag@Cu_2O. (a, b) TEM image. (c) HRTEM image. (d) HAADF-STEM image and corresponding EDS mapping profiles of Cu (e), O (f), and Ag (g). (h) Line scan results of (d). The direction of line scanning is indicated in (d) by a white arrow. From Fig. S3a, it is evident that the core-shell structure of Ag@Cu_2O is uniformly synthesized with a size of approximately 350 nm. Furthermore, Fig. S3b confirms the mesoporous structure of Ag@Cu_2O, as supported by N_2 adsorption-desorption measurements shown in Fig. S4a. The HRTEM image of Ag@Cu_2O (Fig. S3c) validates that the lattice fringe of 0.246 nm corresponds to the (111) plane of Cu_2O, suggesting the Cu_2O composition in Ag@Cu_2O. HAADF-STEM and corresponding EDS mapping images display the spatial element distribution of Ag@Cu_2O, with Ag accumulated at the center of this structure (Fig. S3d-g). Line scan results in Fig. S3h further exhibit the spatial distribution of Cu_2O and Ag, with Ag particles located at the center of the Cu_2O structure.

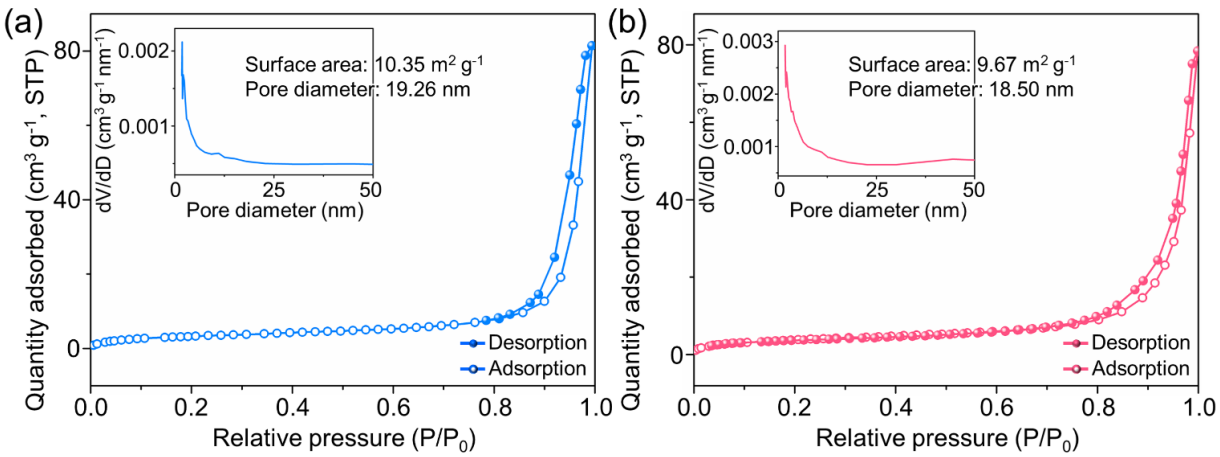

Fig. S4. N_2 adsorption-desorption measurements for Ag@Cu_2O and O-Ag@Cu_2O. N_2 adsorption-desorption isotherms and pore diameter distributions of (a) Ag@Cu_2O and (b) O-Ag@Cu_2O. Type IV curves with H3 hysteresis loops are displayed for both samples, confirming their mesoporous nature. Moreover, both samples display comparable BET surface areas and pore diameter distributions, making the variation in BET surface area and pore size among them negligible. In addition, the pore diameters of the two samples are close to 20 nm, which is very beneficial for substances to enter the catalysts through mesoporous channels. This mesoporous structure enhances the transport of substances in the reaction system, which is beneficial for the reaction.

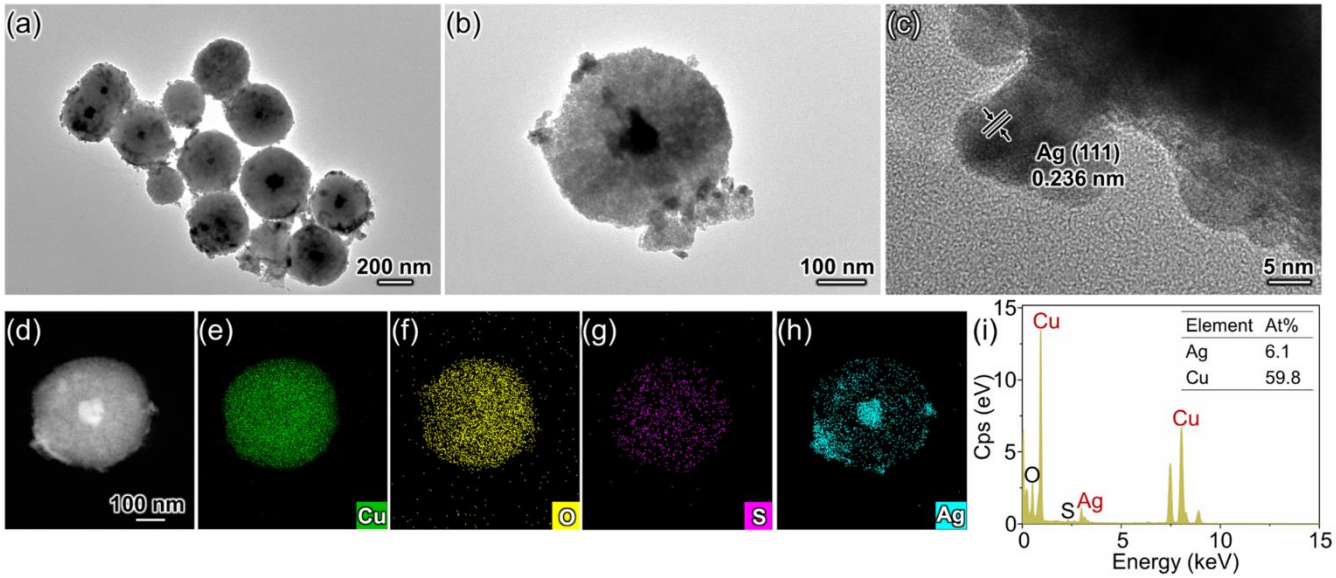

Fig. S5. Ag^+ probe experiment for O-Ag@Cu_2O. (a, b) TEM images. (c) HRTEM image. (d) HAADF-STEM image and corresponding EDS mapping profiles of Cu (e), O (f), S (g), and Ag (h). (i) EDS spectrum of O-Ag@Cu_2O loaded with Ag particles. The inserted table displays the atomic percentages of Cu and Ag elements. TEM images presented in Fig. S5a-b clearly illustrate that some particles are loaded on the surface of O-Ag@Cu_2O. Combined with the lattice fringe of 0.236 nm (Fig. S5c), corresponding to the (111) plane of Ag, it can be confirmed that Ag^+ is reduced to Ag particles by the photogenerated electrons of O-Ag@Cu_2O transferred on the surface. HAADF-STEM and EDS mapping images (Fig. S5d to S5h) further display the distribution of Ag particles on the O-Ag@Cu_2O surface. More importantly, the atomic percentages of Cu and Ag elements shown in Fig. S5i illustrate that the amount of Ag obtained from the reduction of surface photogenerated electrons in the hydrophobically modified sample (O-Ag@Cu_2O) is not less than that of the unmodified sample (Ag@Cu_2O, Fig. S6h). Surface hydrophobic modification appears to have minimal impact on the interaction between photogenerated electrons migrating to the surface and reactants adsorbed there.

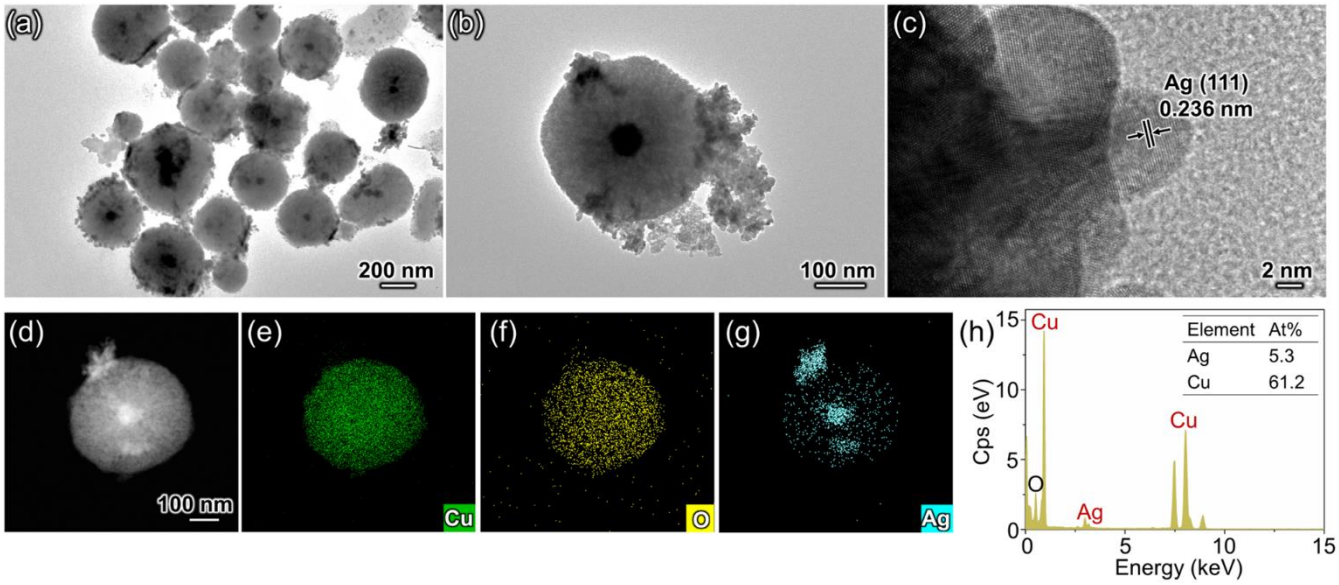

Fig. S6. Ag^+ probe experiment for $Ag@Cu_2O$. (a, b) TEM images. (c) HRTEM image. (d) HAADF-STEM image and corresponding EDS mapping profiles of Cu (e), O (f), and Ag (g). (h) EDS spectrum of $Ag@Cu_2O$ loaded with Ag particles. The inserted table displays the atomic percentages of Cu and Ag elements. Similar to Fig. S5, the TEM and HRTEM images display the reduction of Ag^+ to Ag particles by the photogenerated electrons of $Ag@Cu_2O$ transferred to the surface, which is further proved by the HAADF-STEM and corresponding EDS mapping images.

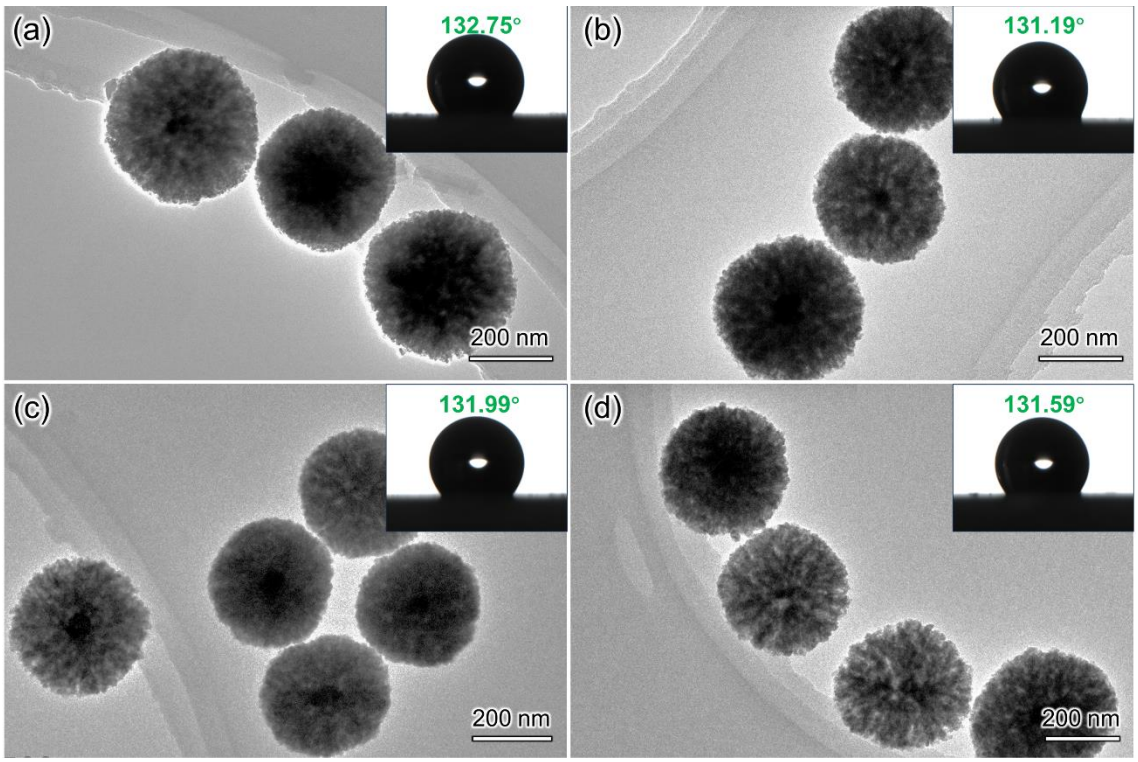

Fig. S7. Morphology of samples obtained under different synthesis scales. (a-d) 100, 400, 800, and 1200 mL, respectively. The inset in each TEM image show the WCA of the corresponding sample. The results show that the morphology and wettability of the samples synthesized at 100 mL (Fig. S7a), 800 mL (Fig. S7c), and 1200 mL (Fig. S7d) scales are consistent with those of the target sample, O-Ag@Cu_2O, synthesized at the 400 mL (Fig. S7b) scale. All samples exhibit a core-shell structure and demonstrate the desired hydrophobic properties, regardless of the synthesis scale. This suggests that the synthesis of the target sample can be appropriately scaled up within the tested range, providing a solid experimental basis for further large-scale production.

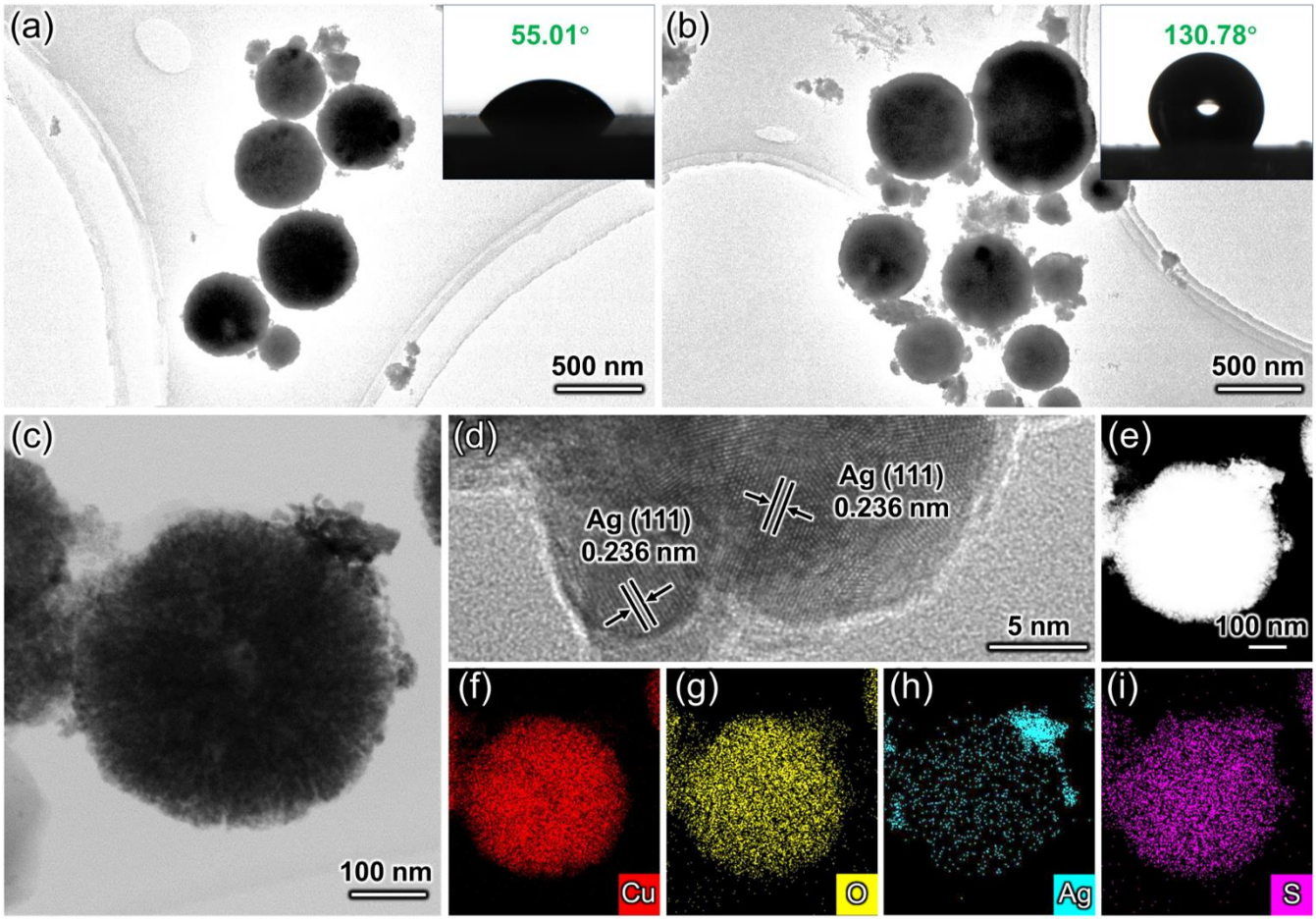

Fig. S8. Morphology and wettability of Ag/Cu_2O and O-Ag/Cu_2O. (a) TEM image of Ag/Cu_2O. Inset is the WCA of Ag/Cu_2O. (b, c) TEM images of O-Ag/Cu_2O. Inset is the WCA of O-Ag/Cu_2O. (d) HRTEM image of O-Ag/Cu_2O. (e) HAADF-STEM image and corresponding EDS mapping profiles of Cu (f), O (g), Ag (h), and S (i). In Fig. S8a, the presence of particles loaded on the surface of Cu_2O is observable, and the synthesized sample demonstrates hydrophilic properties. Following hydrophobic modification, there is no discernible alteration in morphology (Fig. S8b-c). However, the wettability is reversed into hydrophobicity. The HRTEM image of O-Ag/Cu_2O (Fig. S8d) shows that the particles loaded on the catalyst surface exhibit lattice fringes of 0.236 nm, corresponding to the (111) plane of Ag, confirming the successful loading of Ag particles. HAADF-STEM and corresponding EDS mapping images display the spatial distribution of elements within O-Ag/Cu_2O, with Ag primarily accumulating on the Cu_2O surface (Fig. S8e-i). Moreover, the element of S originating from DDT is observed to be uniformly adsorbed on the catalyst surface.

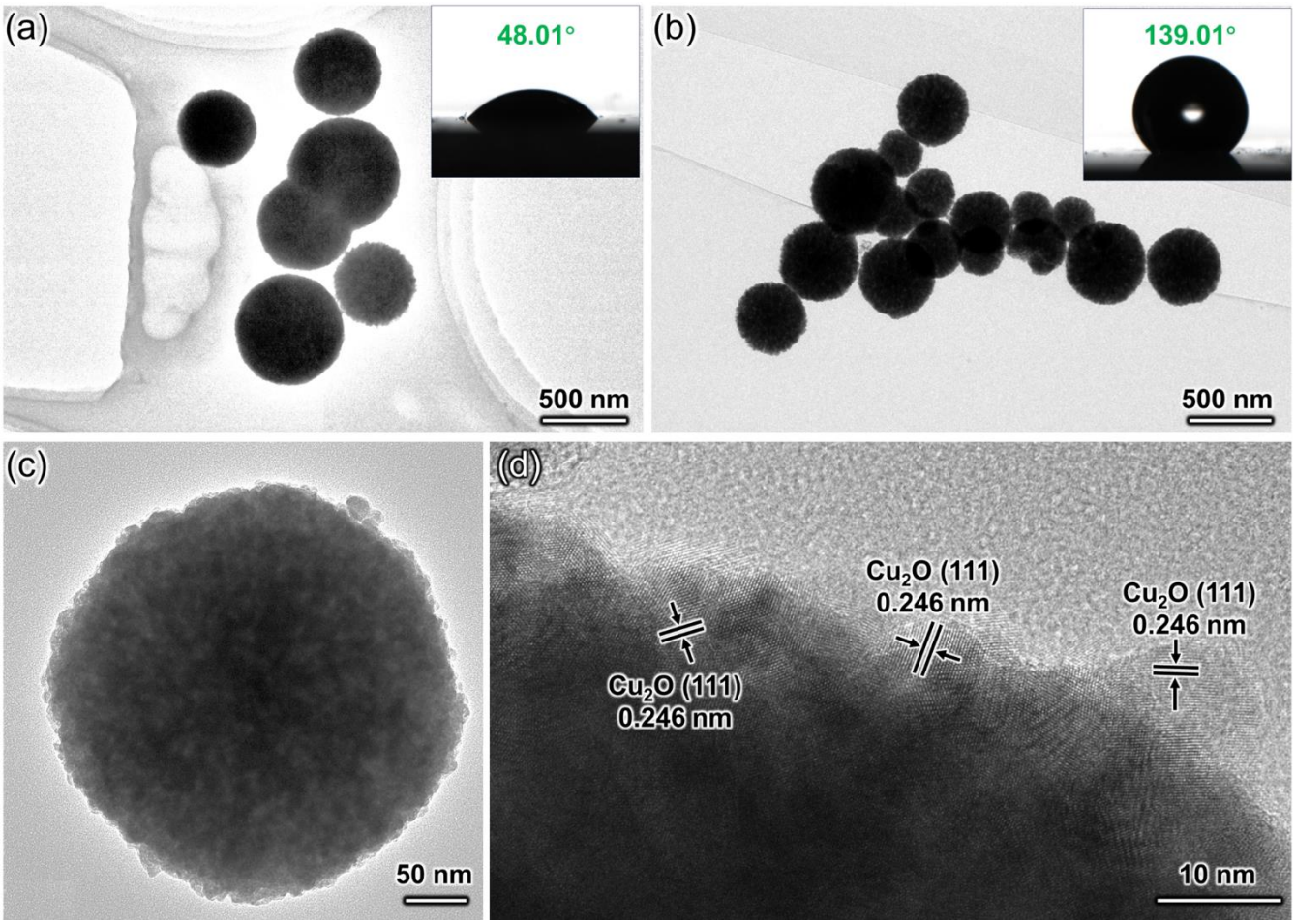

Fig. S9. Morphology and wettability of b-Cu_2O and O-b-Cu_2O. (a) TEM image of b-Cu_2O. Inset is the WCA of b-Cu_2O. (b, c) TEM images of O-b-Cu_2O. Inset is the WCA of O-b-Cu_2O. (d) HRTEM image of O-b-Cu_2O. In Fig. S9a, it is apparent that the synthesized b-Cu_2O exhibits a uniform spherical shape and hydrophilic properties. Following hydrophobic modification, there is no significant change in morphology, however, the wettability is reversed to hydrophobicity (Fig. S9b-c). The HRTEM image of O-b-Cu_2O (Fig. S9d) confirms that the lattice fringes of 0.246 nm correspond to the (111) plane of Cu_2O, suggesting the Cu_2O composition.

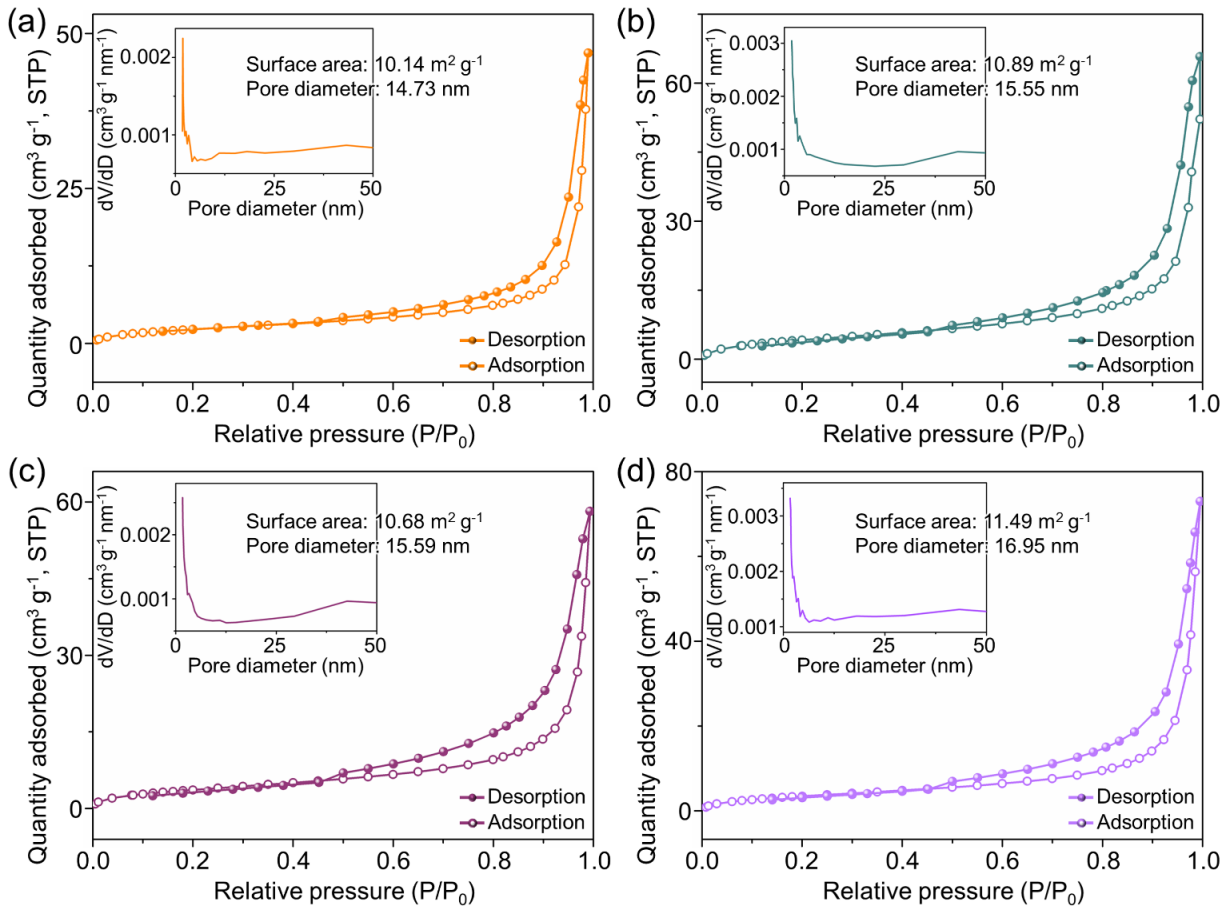

Fig. S10. N_2 adsorption-desorption measurements for O-Ag/Cu_2O, Ag/Cu_2O, O-b-Cu_2O, and b-Cu_2O. N_2 adsorption-desorption isotherms and pore diameter distributions of (a) O-Ag/Cu_2O. (b) Ag/Cu_2O. (c) O-b-Cu_2O. (d) b-Cu_2O. Similar to Fig. S4, type IV curves with H3 hysteresis loops for the four samples also confirm their mesoporous nature. Additionally, the BET surface areas and pore diameter distributions of these four samples exhibit similarity to those of O-Ag@Cu_2O and Ag@Cu_2O, thereby rendering the variation in BET surface area and pore size among the six samples negligible.

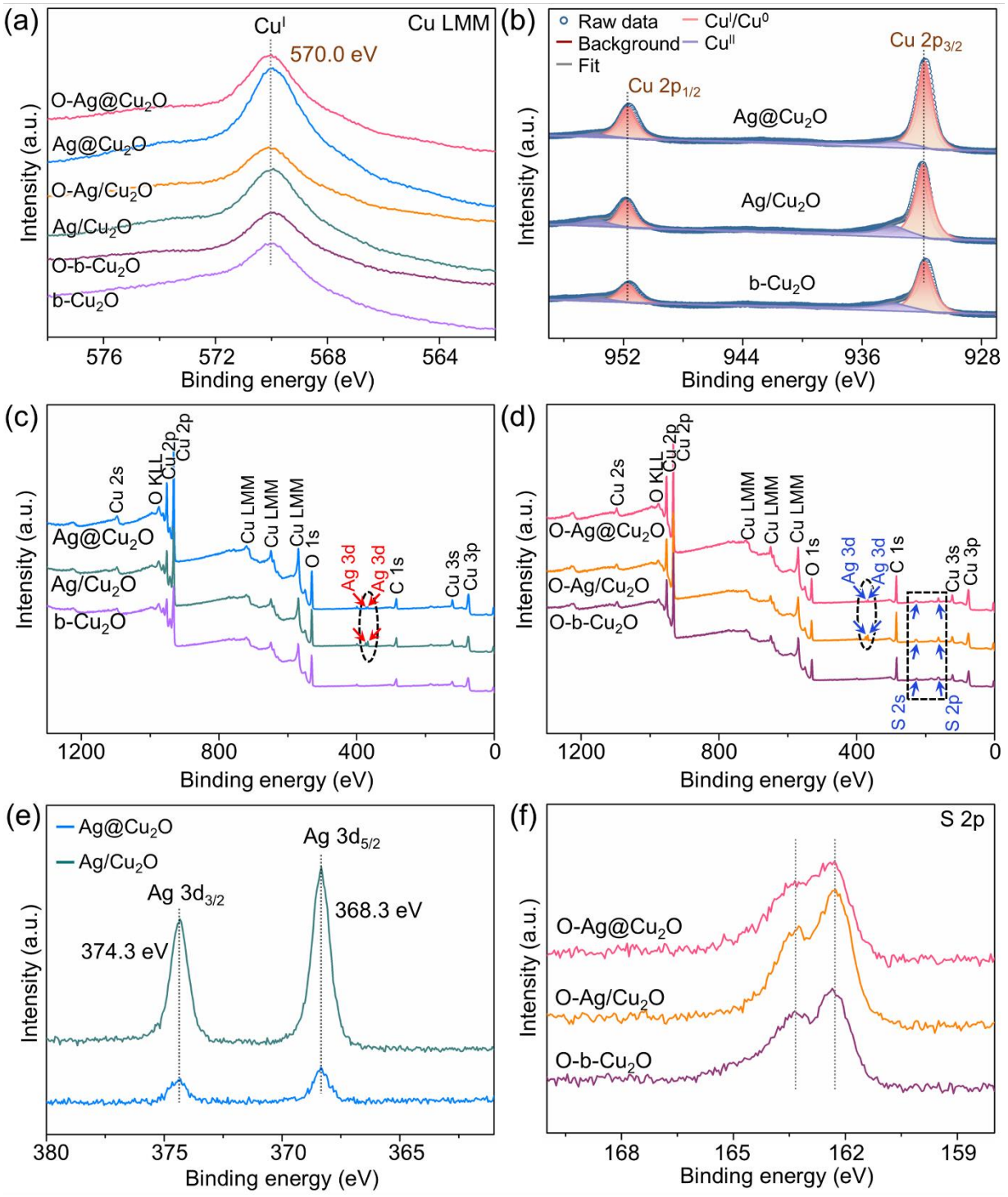

Fig. S11. XPS results. (a) Cu LMM Auger spectra of O-Ag@Cu$_2$O, Ag@Cu$_2$O, O-Ag/Cu$_2$O, Ag/Cu$_2$O, O-b-Cu$_2$O, and b-Cu$_2$O. (b) High-resolution Cu 2p XPS spectra of Ag@Cu$_2$O, Ag/Cu$_2$O, and b-Cu$_2$O. (c) XPS surveys of Ag@Cu$_2$O, Ag/Cu$_2$O, and b-Cu$_2$O. (d) XPS surveys of O-Ag@Cu$_2$O, O-Ag/Cu$_2$O, and O-b-Cu$_2$O. (e) High-resolution Ag 3d XPS spectra of Ag@Cu$_2$O and Ag/Cu$_2$O. (f) Raw data plots of high-resolution S 2p XPS spectra of O-Ag@Cu$_2$O, O-Ag/Cu$_2$O, and O-b-Cu$_2$O. The Cu LMM Auger spectra display a peak at 570.0 eV, corresponding to Cu(I) (Fig. S11a). Furthermore, XPS surveys for Ag@Cu$_2$O and Ag/Cu$_2$O reveal noticeable signals of Ag (Fig. S11c). After hydrophobic modification, the signals of Ag still exist (Fig. S11d). Moreover, the discernible signals of S for O-Ag@Cu$_2$O, O-Ag/Cu$_2$O, and O-b-Cu$_2$O are observed, indicating the presence of DDT on the surface of these materials (Fig. S11d). The raw data plots of high-resolution XPS spectra of S 2p for O-Ag@Cu$_2$O, O-Ag/Cu$_2$O, and O-b-Cu$_2$O all display two prominent peaks with identical peak positions, exhibiting that the state of S is the same for the three samples (Fig. S11f).

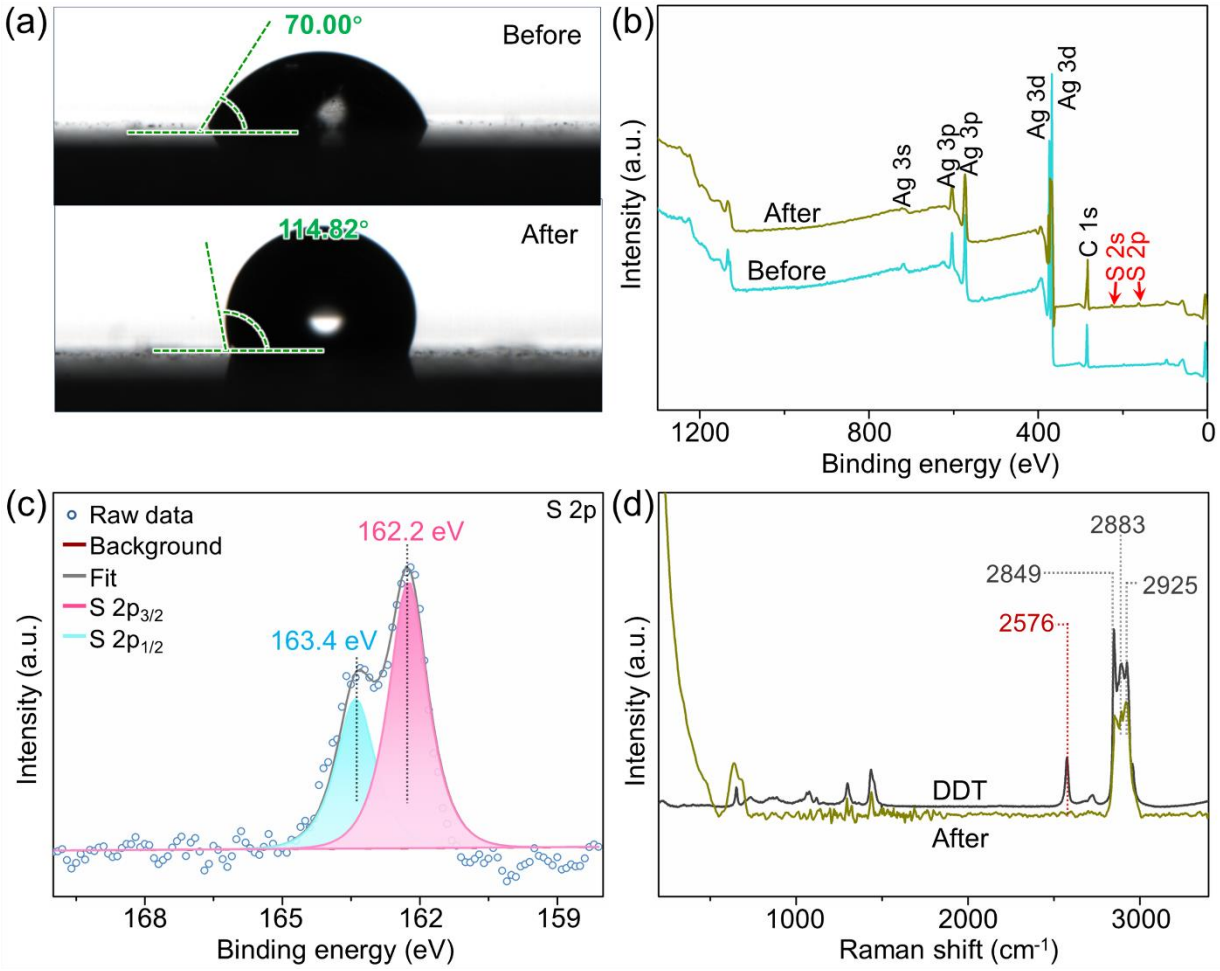

Fig. S12. Characterizations of the interaction between Ag and DDT. (a) WCAs of Ag particles before (up) and after (down) hydrophobic modification. (b) XPS surveys of Ag particles before and after hydrophobic modification. (c) High-resolution S 2p XPS spectrum of Ag particles after hydrophobic modification. (d) Raman spectra of DDT and Ag particles after hydrophobic modification. The synthesized Ag particles underwent the same surface hydrophobic modification procedure used for O-Ag@Cu_2O. The WCAs were measured before and after hydrophobic modification, with the results presented in Fig. S12a. It is evident that the Ag particles exhibit hydrophilicity prior to treatment and become hydrophobic following treatment with DDT. This indicates an effective interaction between DDT and the Ag particles. Further analysis using XPS was conducted on the Ag particles before and after hydrophobic modification, as shown in the XPS surveys in Fig. S12b. After hydrophobic treatment, the presence of a S signal on the Ag particle surfaces, originating from DDT, suggests that DDT is present on the Ag particle surfaces. The high-resolution S 2p XPS spectrum in Fig. S12c exhibits a binding energy of 162.2 eV for S $2p_{3/2}$ peak, which corresponds to the sulfur state typically found in thiolate species.[6] This finding indicates that during the interaction between DDT and the Ag particle surfaces, the thiol bond (-S-H) in DDT breaks, allowing sulfur to form new bonds with Ag atoms and resulting in thiolate formation. Raman spectroscopy further corroborates these conclusions. As shown in Fig. S12d, the Ag particle surfaces after hydrophobic treatment exhibit distinct vibrational signals attributable to the alkyl groups of DDT (-CH_2-: 2849 cm^{-1} and 2925 cm^{-1}; -CH_3: 2883 cm^{-1}),[7] confirming the attachment of DDT to the Ag particle surfaces. Additionally, the characteristic peak of the -S-H bond (2576 cm^{-1}) in DDT disappears,[7] confirming the cleavage of the -S-H bond during the interaction between DDT and Ag particles. Thus, it is demonstrated that DDT can interact with the surfaces of Ag particles.

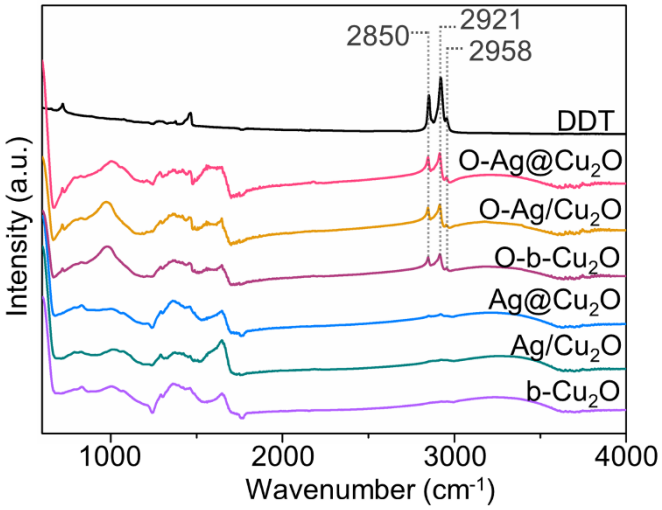

Fig. S13. FTIR spectra of different samples. DDT exhibits distinct peaks at 2850, 2921, and 2958 cm^{-1}, corresponding to the symmetric stretching of -CH_2-, the asymmetric stretching of -CH_2-, and the asymmetric stretching of -CH_3, respectively.[7] After the modification with DDT, these characteristic peaks are evident in O-Ag@Cu_2O, O-Ag/Cu_2O, and O-b-Cu_2O, suggesting the presence of DDT on the surfaces of these three samples.

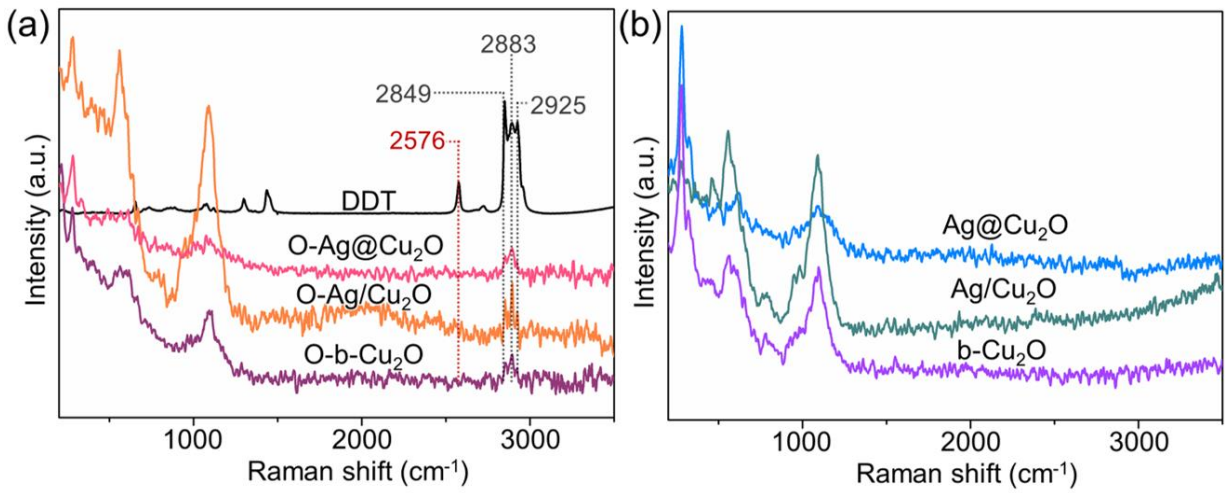

Fig. S14. Raman characterizations. (a) Raman spectra of DDT, O-Ag@Cu_2O, O-Ag/Cu_2O, and O-b-Cu_2O. (b) Raman spectra of Ag@Cu_2O, Ag/Cu_2O, and b-Cu_2O. The Raman spectra further support the evidence of chemical adsorption between DDT and the Cu_2O surface of the catalysts. As depicted in Fig. S14a, DDT exhibits prominent characteristic peaks at 2576, 2849, 2883, and 2925 cm^{-1}, associated with the vibrations of C-H in -CH_2- (2849 and 2925 cm^{-1}), -S-H (2576 cm^{-1}), and C-H in -CH_3 (2883 cm^{-1}), respectively.[7] In contrast, the peaks at 2849, 2883, and 2925 cm^{-1} persist for O-Ag@Cu_2O, O-Ag/Cu_2O, and O-b-Cu_2O, while the peak at 2576 cm^{-1} disappears. This observation indicates that the -S-H in DDT is disrupted upon adsorption onto the surfaces of O-Ag@Cu_2O, O-Ag/Cu_2O, and O-b-Cu_2O, which aligns with the findings from the S 2*p* XPS spectra shown in Fig. 2d.[8]

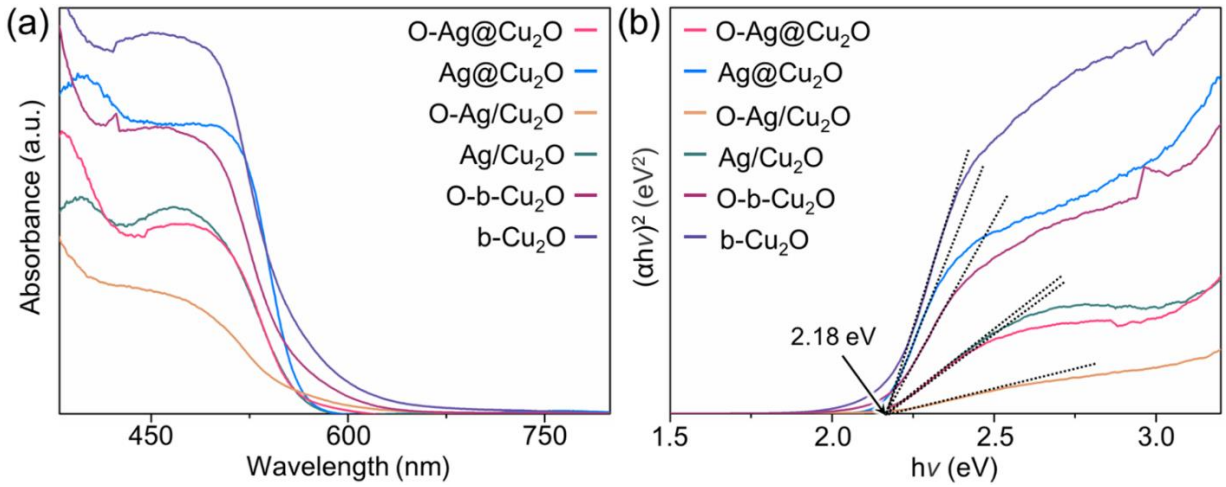

Fig. S15. Light absorption characterizations. (a) UV-vis diffuse reflectance spectra. Reflectivity is directly measured to characterize light absorption with $BaSO_4$ serving as the reference sample. The obtained values are converted into absorbance through the Kubelka-Munk formula built into the instrument. (b) Bandgap determined from the Tauc plots.

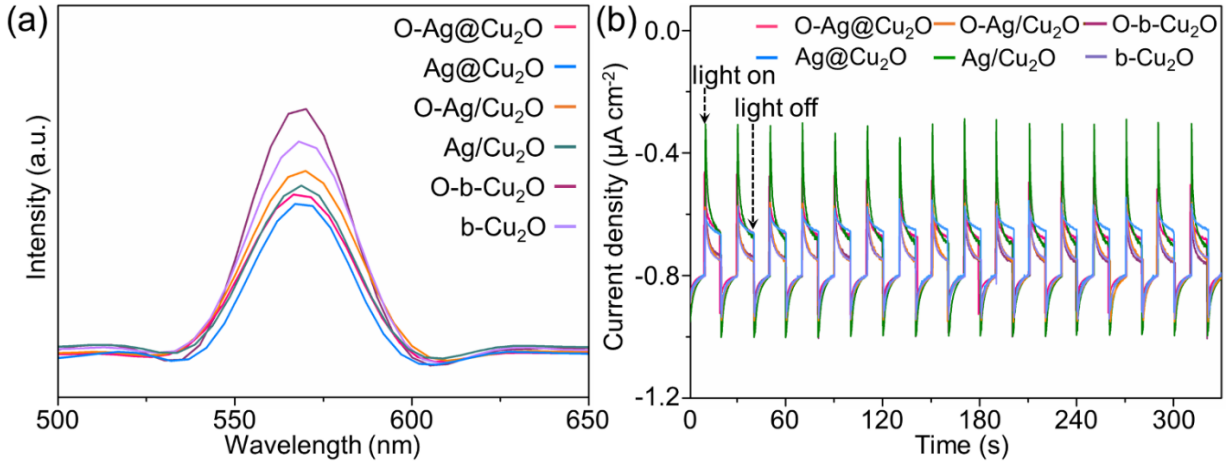

Fig. S16. Photoluminescence (PL) and photocurrent characterizations. (a) Steady-state PL spectra under the excitation wavelength of 405 nm. (b) Transient photocurrent curves with light on/off cycles under visible light irradiation.

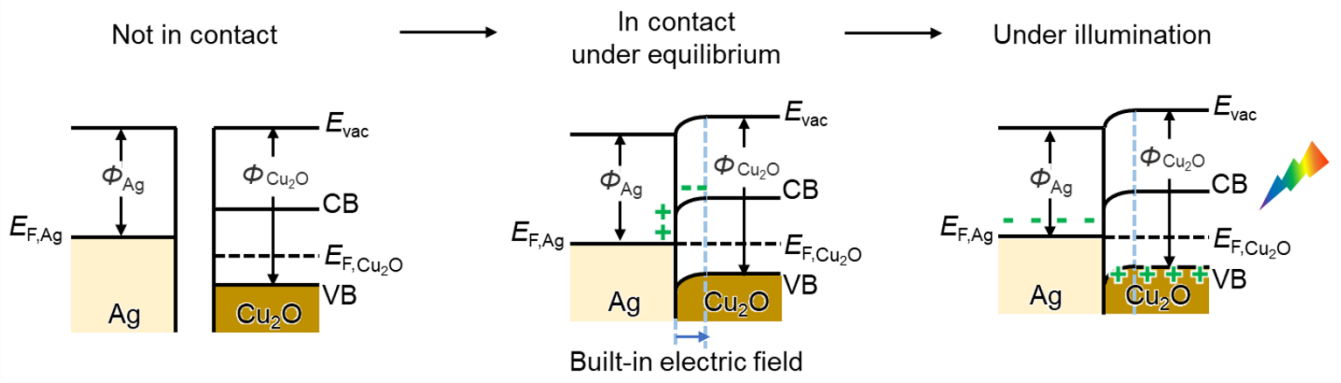

Fig. S17. Energy band diagrams of Ag and Cu_2O contacts. $E_{F,Ag}$: the Fermi level of Ag; E_{F,Cu_2O}: the Fermi level of Ag; E_{vac}: vacuum energy; CB: conduction band; VB: valence band; ϕ_{Ag}: the work function of Ag; ϕ_{Cu_2O}: the work function of Cu_2O. At the interface between Ag and Cu_2O, electron transfer occurs due to the difference in their Fermi levels.[9] Specifically, Cu_2O, being a p-type semiconductor, typically has a lower Fermi level ($\phi_{Cu2O} \approx 4.8$ eV) compared to Ag ($\phi_{Ag} \approx 4.1$ eV).[10-12] Upon initial contact, electrons transfer from Ag to Cu_2O until thermal equilibrium is established, resulting in a charge transfer region and the formation of a built-in electric field directed from Ag to Cu_2O.[12, 13] When the catalyst is exposed to light, Cu_2O generates electron-hole pairs, with photogenerated electrons occupying the CB. The built-in electric field then exerts a force that drives these electrons toward the Ag particles. Additionally, since the bottom of the CB of Cu_2O is higher than the new equilibrium Fermi energy level, the photogenerated electrons ultimately transfer from Cu_2O to Ag particles.[12, 13] Moreover, the photogenerated holes, which can be relatively viewed as positively charged, remain within Cu_2O due to the same electric field, preventing their recombination with electrons and enhancing charge separation efficiency. For areas of the Cu_2O surface not in contact with Ag particles, photogenerated electrons can still migrate to the Cu_2O surface and participate in surface reactions. This is corroborated by the results shown in Fig. S5, where an Ag^+ probe experiment demonstrated that photogenerated electrons from Cu_2O reduce Ag^+ ions to Ag particles on the Cu_2O surface after illumination.

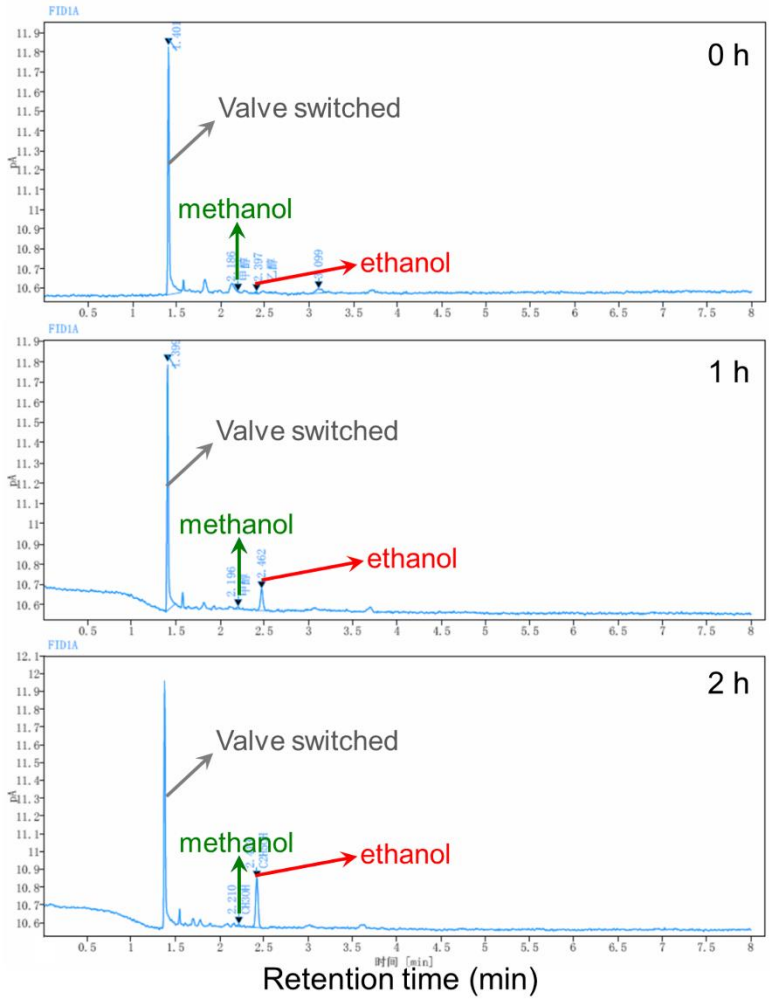

Fig. S18. Original data obtained from gas chromatography (GC). The intensity of characteristic peaks associated with methanol and ethanol exhibits an increase as the reaction progresses. Moreover, the rate of ethanol production demonstrates a significantly faster growth compared to that of methanol, indicating a high selectivity for ethanol production.

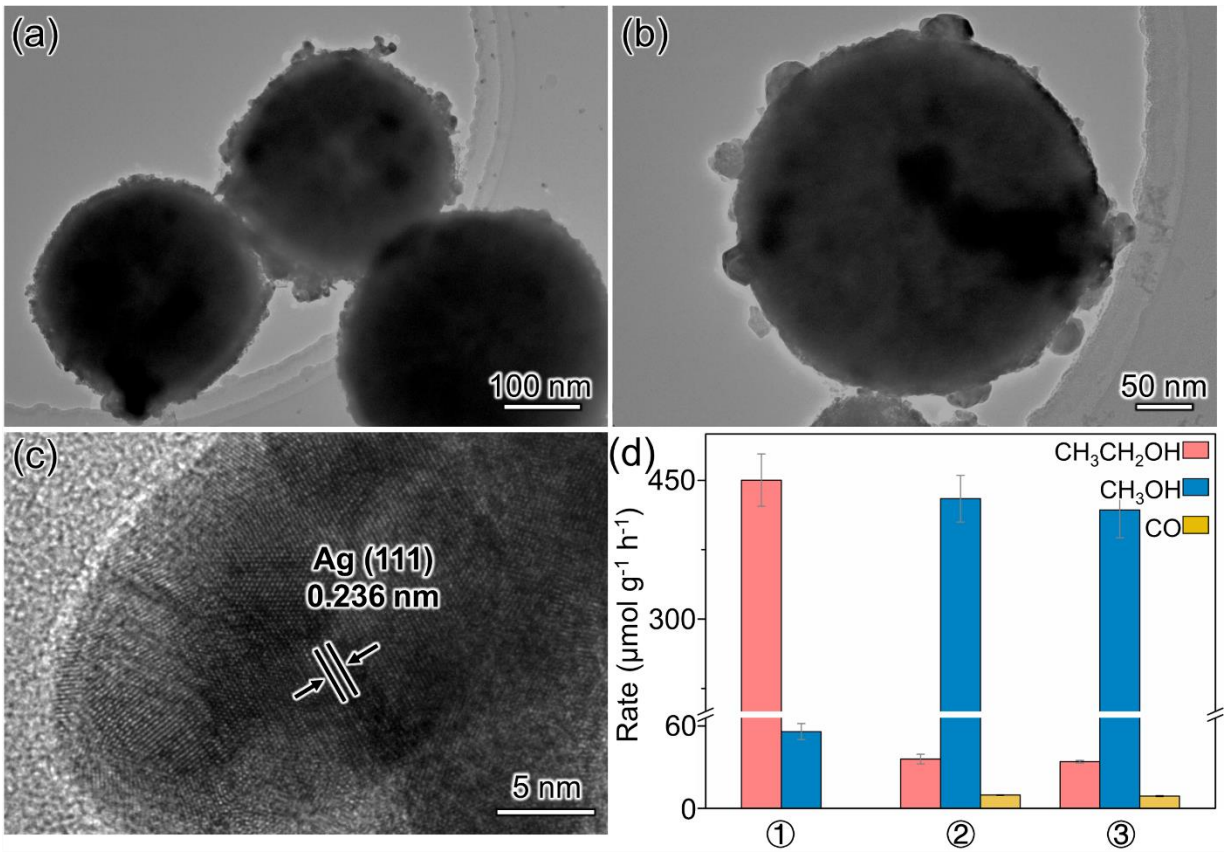

Fig. S19. Supplementary PCRR performance. (a, b) TEM images of O-Ag/Cu_2O with increased Ag particle size. (c) HRTEM images of O-Ag/Cu_2O with increased Ag particle size. (d) Generation rates of carbonaceous products for ① O-Ag@Cu_2O, ② O-Ag/Cu_2O, ③ O-Ag/Cu_2O with increased Ag particle size. To further rule out the possibility that the significant performance difference between O-Ag/Cu_2O and O-Ag@Cu_2O arises from the different sizes of Ag particles in the catalysts, the Ag particle size in the comparative catalyst O-Ag/Cu_2O was adjusted to match that in O-Ag@Cu_2O. Specifically, by strategically prolonging the photodeposition duration and increasing the quantity of the precursor $AgNO_3$, the size of Ag particles within O-Ag/Cu_2O was augmented. As evident from Fig. S19b, the size of the deposited Ag particles expanded to approximately 40 nm, which is commensurate with the size of Ag particles within O-Ag@Cu_2O. Furthermore, the lattice spacing discerned from the HRTEM analysis in Fig. S19c validates the successful loading of Ag particles. Subsequently, the catalytic performance of O-Ag/Cu_2O with increased Ag particle size was evaluated for CO_2 reduction, and the results are presented in Fig. S19d. It was found that when the Ag particle size in O-Ag/Cu_2O was increased, its performance did not improve; in fact, it slightly decreased.[14] This outcome could be attributed to the fact that larger particles reduce the proportion of atoms exposed at corners and edges, which are critical active sites due to their higher surface energy and lower coordination number.[15] As a result, the decrease in available active sites led to a reduction in catalytic performance. Therefore, even when the Ag particles in O-Ag/Cu_2O were sized similarly to those in O-Ag@Cu_2O, the performance of O-Ag/Cu_2O remained significantly lower than that of O-Ag@Cu_2O. This finding demonstrates that the superior performance of O-Ag@Cu_2O is not primarily due to the size of the Ag particles, laying the groundwork for further exploration into the true factors driving its exceptional performance.

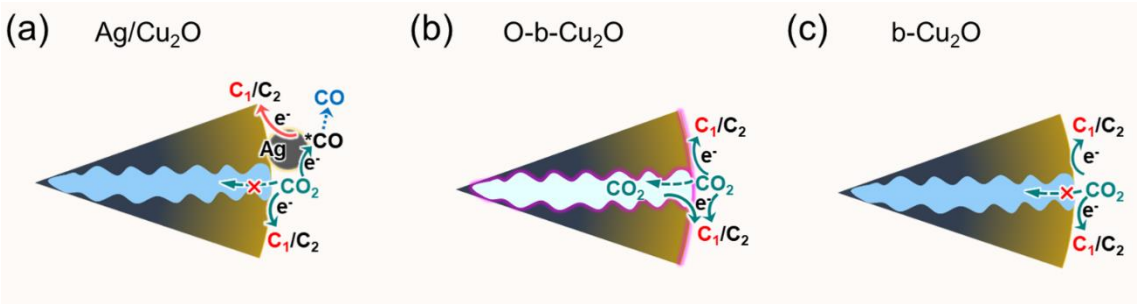

Fig. S20. Schemes of the PCRR for different structures. (a) Ag/Cu_2O. (b) O-b-Cu_2O. (c) b-Cu_2O. In comparison to b-Cu_2O, the presence of the Ag cocatalyst on Ag/Cu_2O enhances the PCRR process, leading to the generation of CO (Fig. S20a and S20c). Subsequently, the CO molecules re-adsorb on the Cu_2O surface, promoting the continuation of the PCRR. Additionally, the produced CO can diffuse directly into the surrounding environment. On the other hand, O-b-Cu_2O, exhibiting hydrophobic characteristics, can capture more CO_2 on its outer surface and within the mesoporous channels of Cu_2O when compared to b-Cu_2O (Figs. S20b-c). This accumulation results in an increased number of reactive sites and available reactant CO_2 for the PCRR process.

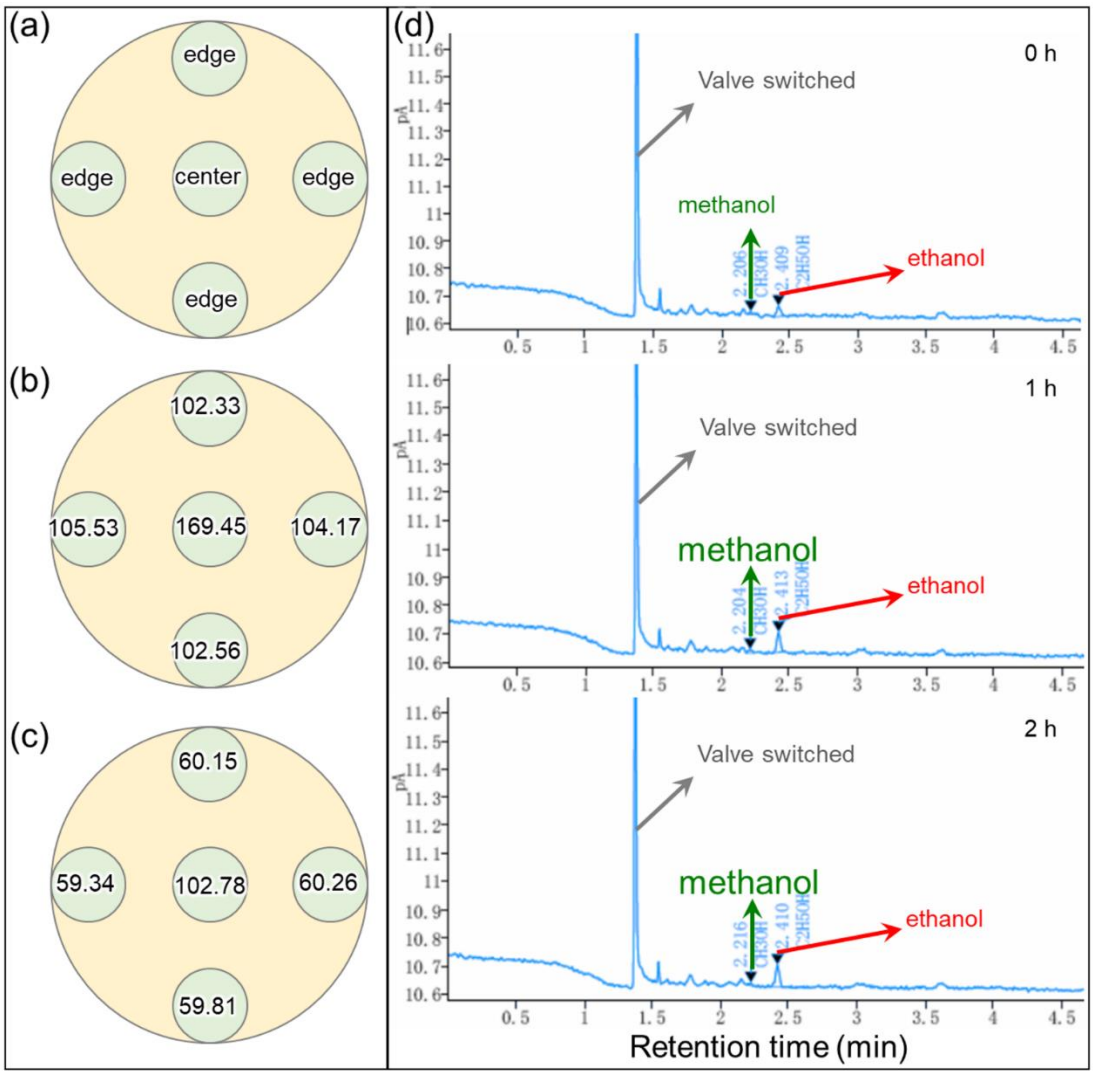

Fig.S21. Light intensity test and original data obtained from GC. (a) Five different light test positions. (b, c) Corresponding test values of a 300 W Xe lamp with a 420 nm filter and a 300 W Xe lamp with a 420 nm bandpass filter, respectively. The unit of light intensity is mW cm^{-2}. (d) Original data obtained from GC under 420 nm irradiation over O-Ag@Cu_2O. As shown in Fig. S21d, it can be seen that upon exposure to 420 nm, there is an increase in the peak area corresponding to ethanol. This observation once again verifies the good activity of O-Ag@Cu_2O in producing ethanol under visible light irradiation.

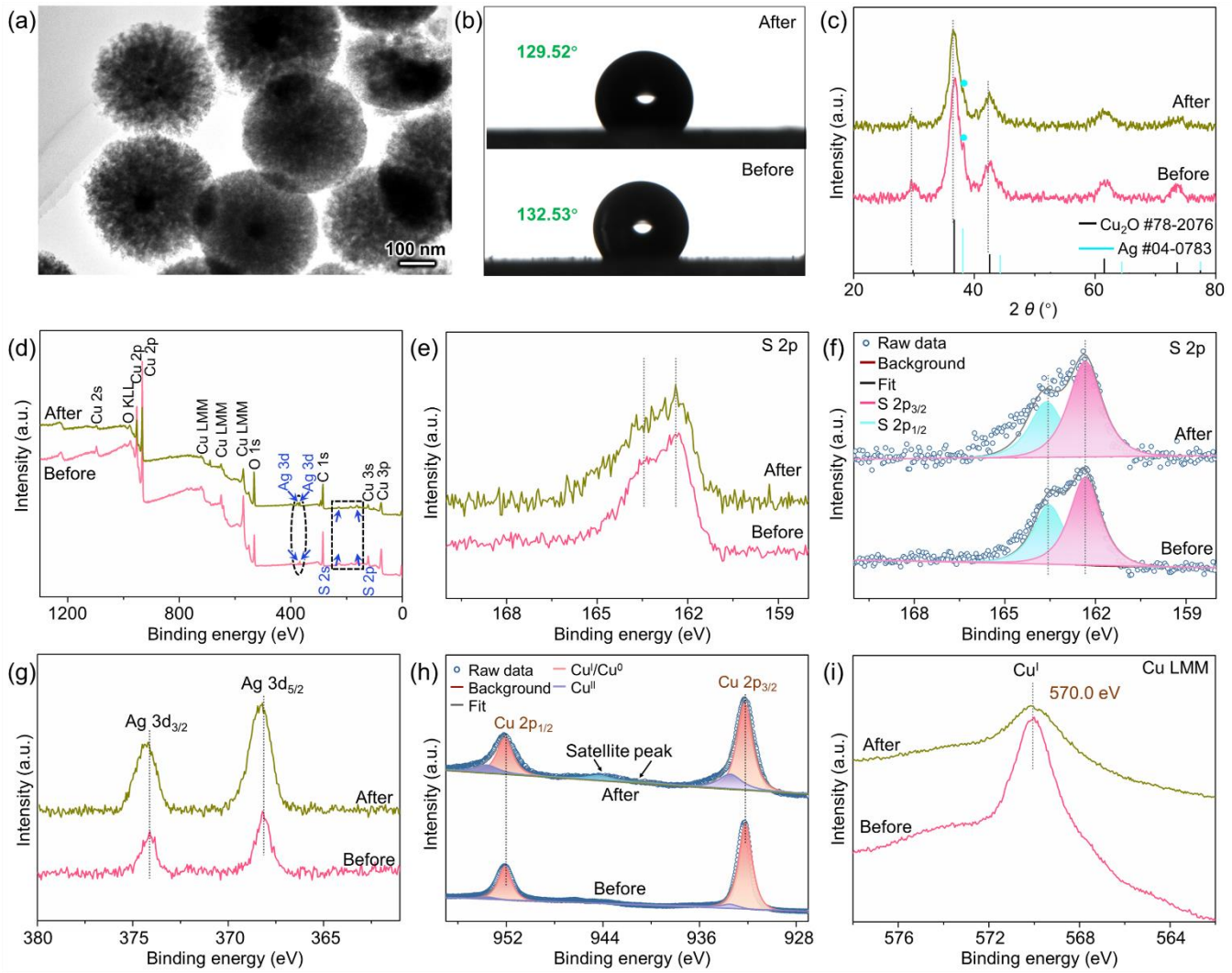

Fig. S22. Characterizations of O-Ag@Cu_2O before and after the reaction of recycle experiments. (a) TEM image of O-Ag@Cu_2O after the reaction. (b) WCAs of O-Ag@Cu_2O before (up) and after (down) the reaction. (c) XRD patterns, (d) XPS surveys, (e) Raw data plots of high-resolution XPS spectra of S 2p, (f) High-resolution XPS spectra of S 2p, (g) High-resolution XPS spectra of Ag 3d, (h) High-resolution Cu 2p XPS spectra, and (i) Cu LMM Auger spectra of O-Ag@Cu_2O before and after the reaction, respectively. The TEM image of the spent O-Ag@Cu_2O illustrates that there is no significant alteration in the core-shell structure following a 12-hour reaction (Fig. S22a). Additionally, the WCA of the spent O-Ag@Cu_2O is measured to be 129.52°, which closely resembles the WCA of O-Ag@Cu_2O before the reaction, indicating its good wettability stability during the PCRR (Fig. S22b). To investigate any structural and compositional changes in O-Ag@Cu_2O after the reaction, XRD and XPS measurements are performed. The comparable XRD patterns obtained before and after the reaction indicate that the crystal structure and composition of O-Ag@Cu_2O remain unchanged throughout the reaction (Fig. S22c). Moreover, both the S 2p and Ag 3d XPS spectra exhibit no discernible variations, indicating that the presence state of DDT and Ag in the structure of O-Ag@Cu_2O remains unaltered (Fig. S22d-g). The Cu 2p XPS spectra (Fig. S22h) exhibit a slight increase in Cu^{II} signals accompanied by weak-intensity satellite peaks, suggestive of minor oxidation on the catalyst surface.[16] Nonetheless, the primary component of the catalyst continues to be Cu_2O. Overall, there are no significant changes observed in the morphology, structure, or composition of O-Ag@Cu_2O, implying its better stability.

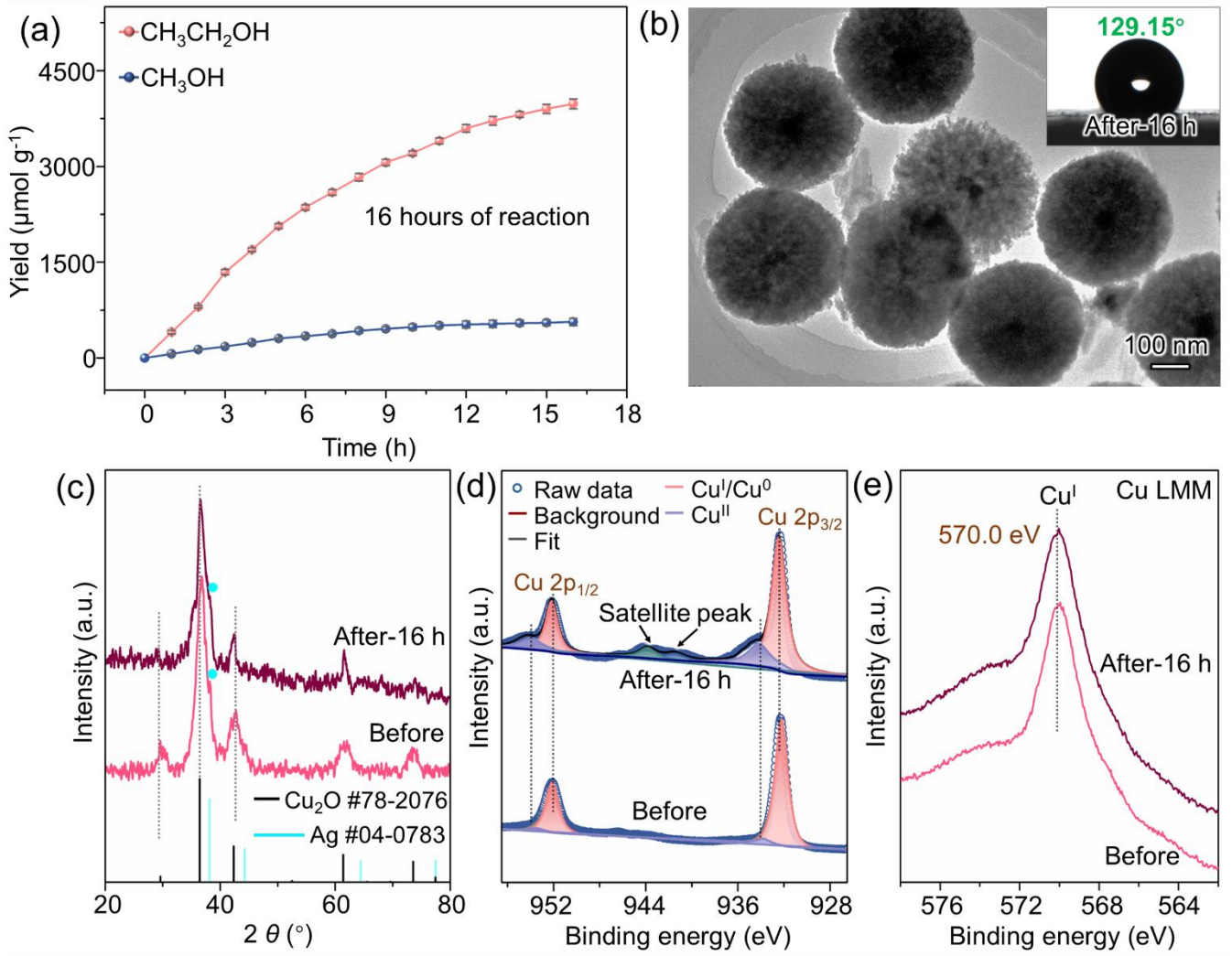

Fig. S23. Supplementary photocatalytic performance of O-Ag@Cu_2O and characterizations of O-Ag@Cu_2O after 16 hours of continuous reaction. (a) Ethanol and methanol yields over time. (b) TEM image of O-Ag@Cu_2O after 16 hours of continuous reaction. Inset is the WCA of O-Ag@Cu_2O after 16 hours of continuous reaction. (c) XRD patterns, (d) High-resolution Cu 2p XPS spectra, and (e) Cu LMM Auger spectra of O-Ag@Cu_2O before and after 16 hours of continuous reaction. As depicted in Fig. S23a, the production of ethanol and methanol exhibits an initial steady increase, followed by a slight deceleration in the growth rate as the photocatalytic reaction progresses. To gain a profound understanding of the long-term performance of O-Ag@Cu_2O, a suite of characterizations including TEM, XRD, WCA, and XPS were conducted for O-Ag@Cu_2O after 16 hours of reaction. The TEM image confirms the preservation of the core-shell structure (Fig. S23b). Additionally, the catalyst maintains its hydrophobic properties, exhibiting a WCA of 129.15°, similar to that observed before the reaction. The XRD pattern shows that the primary peaks align with the characteristic peaks of cubic phase Cu_2O (JCPDS Card No. 78-2076) (Fig. S23c), indicating that the predominant Cu-containing component remains Cu_2O even after 16 hours of reaction. Notably, no characteristic peaks of Cu are detected, confirming the stability of the Cu_2O phase. Additionally, the presence of Ag signals in the XRD pattern suggests that there are no significant changes to the Ag particles within O-Ag@Cu_2O. Furthermore, the high-resolution Cu 2p XPS spectra of O-Ag@Cu_2O illustrate that, compared to O-Ag@Cu_2O before the reaction, the difference for O-Ag@Cu_2O after 16 hours of reaction is in the intensity of Cu^{II} signals, with stronger Cu^{II} signals accompanied by satellite peaks for the latter (Fig. S23d).[16] Moreover, the Cu LMM Auger spectra for O-Ag@Cu_2O after 16 hours of reaction remain similar to that of O-Ag@Cu_2O before the reaction, with no signals indicative of Cu^0 (Fig. S23e). The results from both XRD and XPS characterizations imply that Cu_2O within O-Ag@Cu_2O experiences a degree of oxidation during the reaction. The prevailing deactivation pathway for O-Ag@Cu_2O appears to involve the photooxidation of Cu_2O by photogenerated holes, which aligns with existing literature findings.[17] This deactivation pathway follows the chemical equation: $Cu_2O + 2OH^- + 2h^+ \rightarrow 2CuO + H_2O$.[18]

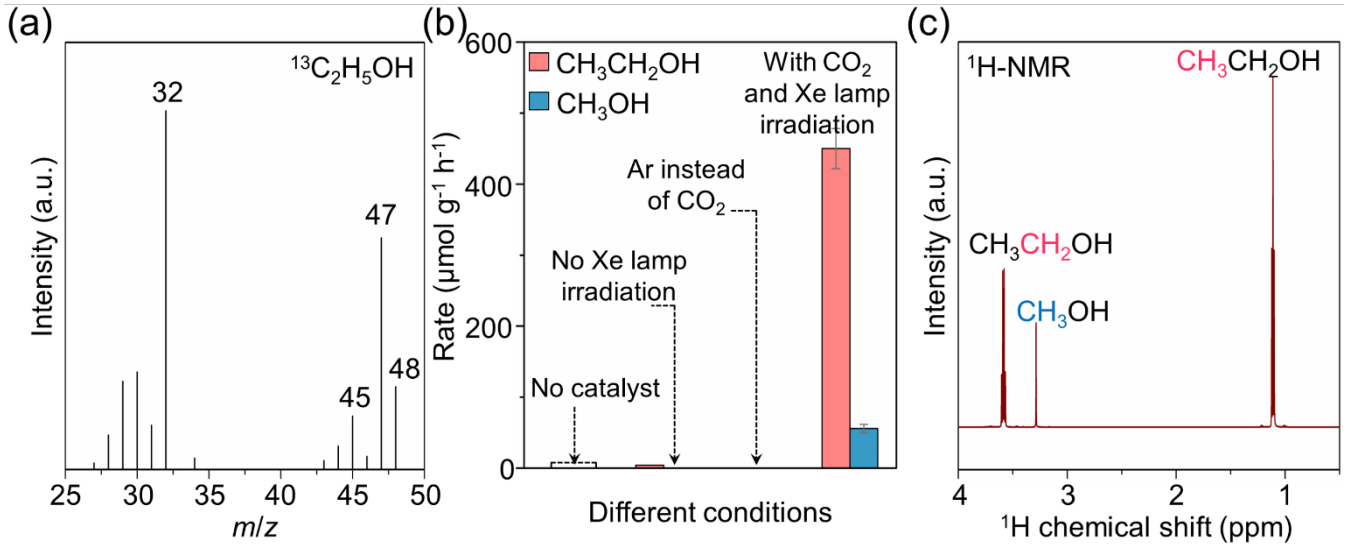

Fig. S24. Supplementary PCRR performance. (a) GC-MS analytical data for ^{13}C isotope-tracing experiment for ethanol detection over O-Ag@Cu_2O. (b) Control experiments. (c) ^{1}H-NMR chemical shift (δ) positions of possible PCRR products over O-Ag@Cu_2O. Several control experiments were conducted to ensure that obtained products originated from the PCRR (Fig. S24b). Firstly, a test was performed using CO_2 and H_2O as reactants in the absence of a photocatalyst. No carbon derivatives were detected in this scenario, indicating that the PCRR could not proceed without the presence of a photocatalyst. When the experiment was repeated with the catalyst and CO_2 but without Xe lamp irradiation, only trace amounts of carbon derivatives were obtained, which may result from natural light-induced PCRR. Moreover, when the reactor was evacuated and purged Ar instead of CO_2, no carbon derivatives were detected under light irradiation in the presence of water and the catalyst, confirming that CO_2 served as the primary carbon source for ethanol and methanol production in the PCRR. Furthermore, as illustrated in Fig. S24c, a triplet is observed at δ ≈ 1.2 ppm, corresponding to the signal of the methyl protons (CH_3) in the ethanol molecule.[19] A quartet is observed at δ ≈ 3.6 ppm, attributed to the methylene protons (CH_2) in ethanol.[20] Additionally, a singlet is observed at δ ≈ 3.3 ppm, corresponding to the methyl protons (CH_3) in the methanol molecule.[21] No additional signals are observed, which strongly indicates that the only carbon-containing products from the PCRR are methanol and ethanol, with no other products such as formic acid or formaldehyde detected.

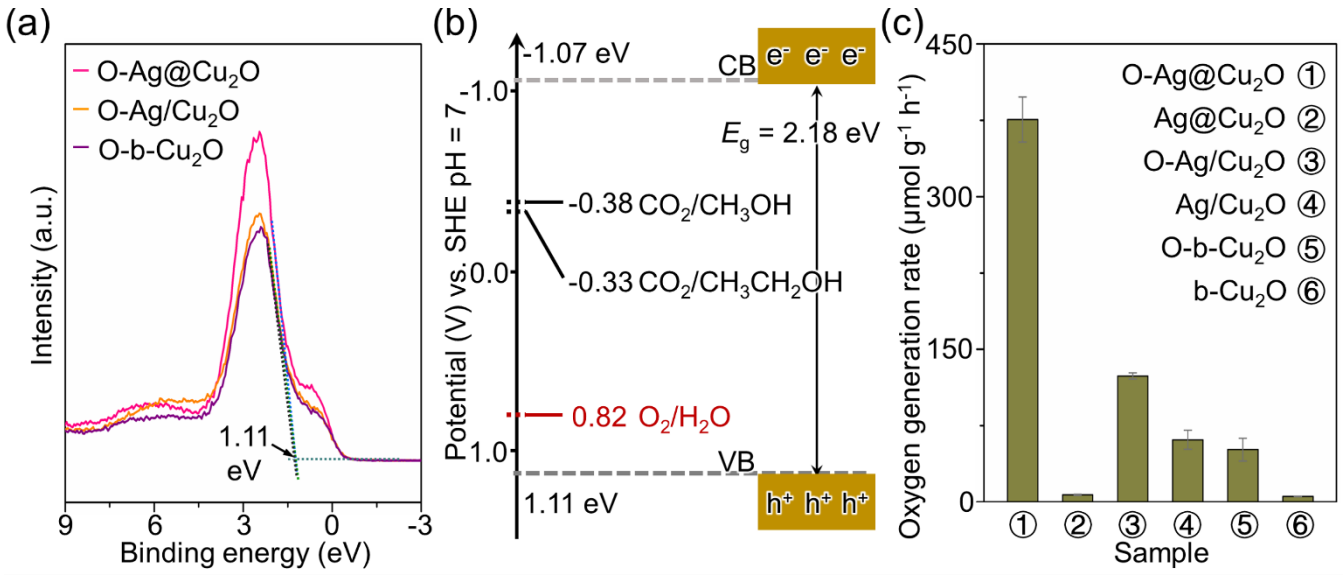

Fig. S25. Oxygen generation performance. (a) Valence-band XPS spectra of O-Ag@Cu_2O, O-Ag/Cu_2O, and O-b-Cu_2O. (b) Band-structure diagram of the designed Cu_2O-based catalyst along with the thermodynamic potentials for CO_2-to-fuel conversion and H_2O oxidation. (c) Rates of oxygen generation in the PCRR.

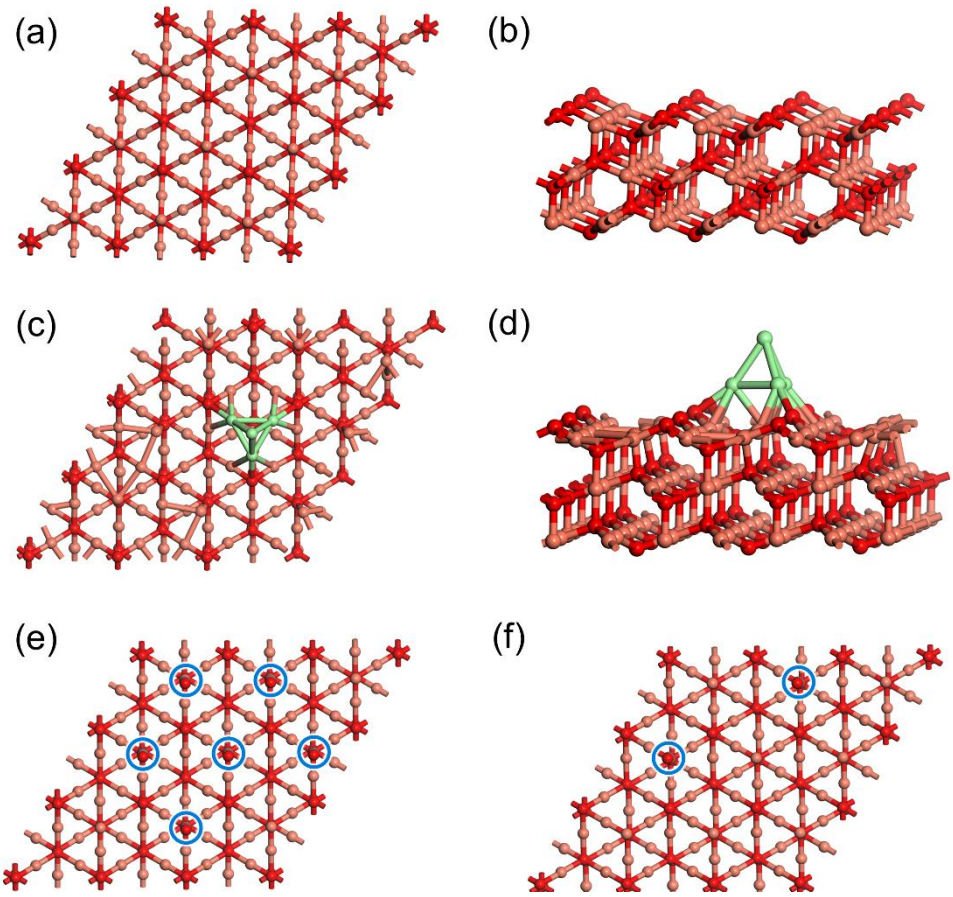

Fig. S26. Different models. (a, b) Top and side views of the slab model of the bare Cu_2O (111) surface (designated as Cu_2O), respectively. (c, d) Top and side views of the slab model of the Cu_2O (111) surface with Ag particles (designated as Ag-Cu_2O), respectively. (e) Configuration of the Cu_2O (111) surface at elevated *CO concentration. (f) Configuration of the Cu_2O (111) surface at low *CO concentration. The brown, gray, red, and green balls represent Cu, C, O, and Ag atoms, respectively.

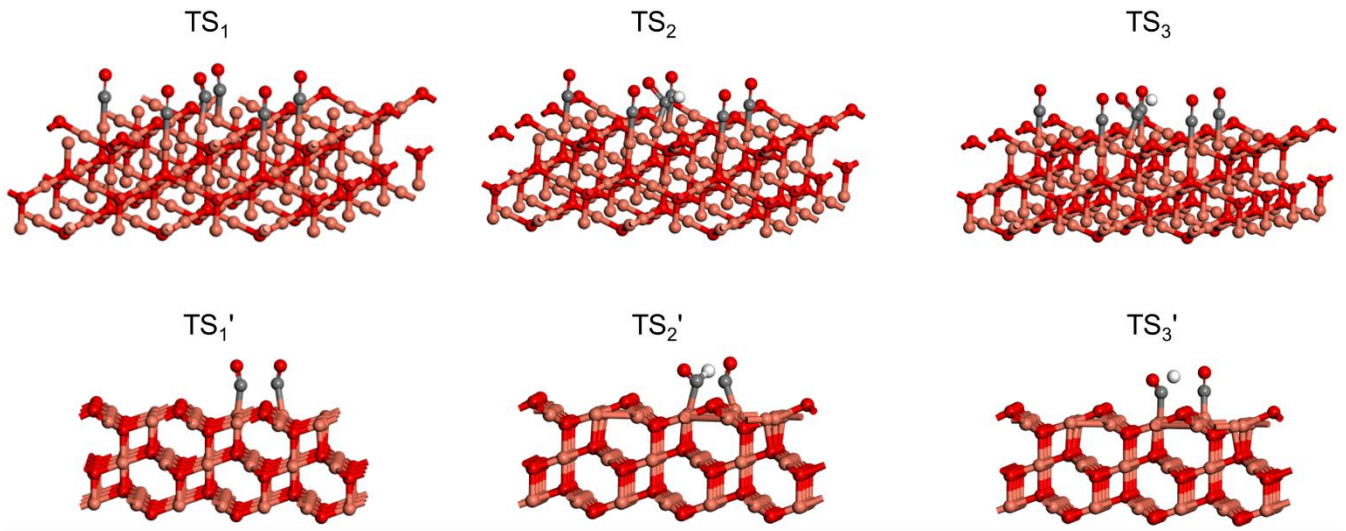

Fig. S27. Different transition state configurations. TS_1, TS_2, and TS_3 represent the transition states of *CO-*CO, *CO-CHO, and *CHO, respectively, at elevated *CO concentration. TS_1', TS_2', and TS_3' represent the transition states of *CO-*CO, *CO-CHO, and *CHO, respectively, at low *CO concentration.

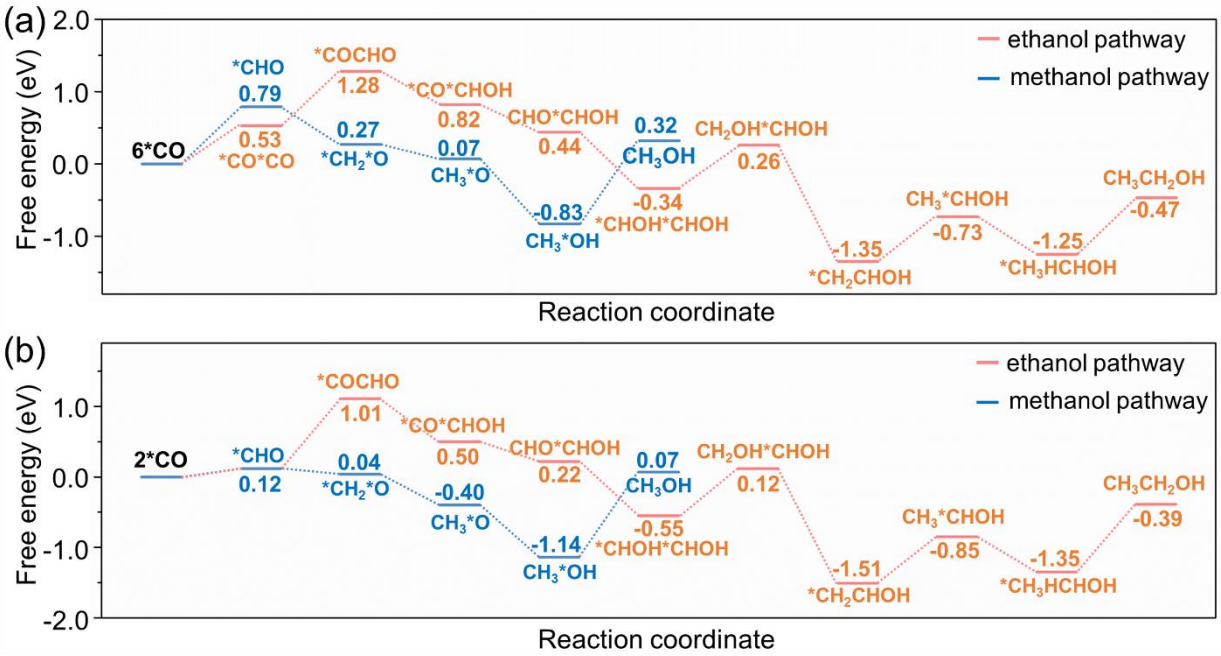

Fig. S28. Reaction pathways of CO_2-to-ethanol and CO_2-to-methanol conversions at different *CO concentrations. (a) At elevated *CO concentration. (b) At low *CO concentration. In our previous research,[22] we meticulously calculated the potential reaction pathways for the conversion of CO_2 to ethanol and CO_2 to methanol under different *CO concentrations using the Cu_2O (111) surface model. Due to the utilization of the similar model in this study as in our prior work,[22] the reaction pathways for the CO_2-to-ethanol and CO_2-to-methanol processes were selected based on the similar methodologies as before. The calculation results for each step are presented in Fig. S28. Notably, at elevated *CO concentration, the *CH_3CH_2OH desorption step and the *CH_3OH desorption step exhibit the highest energy barriers for ethanol and methanol formation, respectively, designating these steps as the rate-determining steps in their respective processes. In contrast, at low *CO concentration, the C-C (*COCHO) coupling step and the *CH_3OH desorption step manifest the maximum energy barriers for ethanol and methanol formation, respectively, thus serving as the rate-determining steps in this situation. Specifically, the energy barrier of the rate-determining step for ethanol formation is reduced by 0.21 eV at elevated *CO concentration compared to that at low *CO concentration. Similarly, for methanol formation, the energy barrier of the rate-determining step is reduced by 0.06 eV at elevated *CO concentration than that presented at low *CO concentration. These findings suggest that elevating *CO concentration promotes both ethanol and methanol formation, thereby indicating that elevating *CO concentration enhances the PCRR. More importantly, elevating *CO concentration significantly lowers the energy barrier of C-C coupling and the rate-determining step for ethanol formation, remarkably facilitating ethanol production.

Table S1. Inductively coupled plasma-optic emission spectroscopy (ICP-OES) testing results.

Element	O-Ag@Cu_2O	O-Ag/Cu_2O
Cu (wt%)	75.050	75.812
Ag (wt%)	2.032	2.027

Table S2. Comparison of the photocatalytic performance of O-Ag@Cu_2O to existing photocatalysts in ethanol production from CO_2 and H_2O.

Year	Photocatalyst	Selectivity (%)	Generation rate (μmol g^{-1} h^{-1})	Ref.
2024	**O-Ag@Cu_2O**	**94.15**	**450.19**	**This work**
2024	Pt_1Ag_{24}-Fe polyphthalocyanine	56	32.97	[19]
2024	$Rh_{0.11}$@Pb_3I_4(^-O_2C-(CH_2NHCH_2)CO_2^-)	89.4	50.5	[23]
2024	Superhydrophobic Cu_2O hollow structure	59.59	996.18	[22]
2024	Alternately hydrophobic TiO_2-Au@Cu_2O	55.77	271.44	[24]
2024	Cu-N_2-V[a]	97.8	69.8	[25]
2024	Cu/NH_2-HKUST-1@TiO_2	94.2	1.29	[26]
2023	Cu@TCPP_0.1	76	491	[27]
2023	In_2O_3/Cu-O_3	85.5	20.7	[28]
2023	1%Co_3O_4/TiO_2	28.8	1.997	[29]
2022	InCu/PCN	92	28.5	[30]
2022	$SrTiO_3$(LaCr)/Cu@Ni/TiN	79	21.3	[31]
2022	$Bi_{19}S_{27}Cl_3$	85	5.19	[32]
2022	Cu/Cd0.5Zn0.5S	31	6.54 μmol h^{-1}	[33]
2021	Bi@Bi_2MoO_6	92.5	17.93	[34]
2020	Cu single-atom/UiO-66-NH_2	61.3	4.22	[35]

[a] Cu-N_2-V: Carbon nitride supported Cu single-atom catalyst featuring defected low-coordination Cu-N_2.

Table S3. Thermochemical data of the reactants and products for the overall PCRR.

Compound	Chemical formula	$\Delta_f G_i^{\ominus}$ (kJ mol^{-1})
Methanol	CH_3OH	−166.3
Ethanol	CH_3CH_2OH	−174.8
Carbon dioxide	CO_2	−394.4

Compound	Chemical formula	$\Delta_f G_i^{\ominus}$ (kJ mol^{-1})
Carbon monoxide	CO	−137.2
Oxygen	O_2	0
Water	H_2O	−237.1

Table S4. Measured *P*, calculated *R*(CH_3OH), *R*(CH_3CH_2OH), and AQE at a wavelength of 420 nm over O-Ag@Cu_2O

λ (nm)	420
P (mW cm^{-2})	74.19
R(CH_3OH) (μmol h^{-1})	6.81
R(CH_3CH_2OH) (μmol h^{-1})	49.3
AQE (%)	3.44

References

1. S. Bai, H. Qiu, M. Song, G. He, F. Wang, Y. Liu and L. Guo, *eScience*, 2022, **2**, 428-437.
2. P.-L. Wang, W. Zhang, Q. Yuan, T. Mai, M.-Y. Qi and M.-G. Ma, *J. Colloid Interface Sci.*, 2023, **645**, 306-318.
3. W. M. Haynes, *CRC handbook of chemistry and physics*, CRC, 2016.
4. G. Kresse and J. Hafner, *Phys. Rev. B*, 1993, **48**, 13115.
5. G. Kresse and J. Furthmüller, *Comp. Mater. Sci.*, 1996, **6**, 15-50.
6. D. Wakerley, S. Lamaison, F. Ozanam, N. Menguy, D. Mercier, P. Marcus, M. Fontecave and V. Mougel, *Nat. Mater.*, 2019, **18**, 1222-1227.
7. J. G. Speight, McGraw-Hill New York, 2005, ch. 3, pp. 3.3-3.50.
8. L. Jiang, T. You, P. Yin, Y. Shang, D. Zhang, L. Guo and S. Yang, *Nanoscale*, 2013, **5**, 2784-2789.
9. Z. Zhang and J. T. Yates, *Chem. Rev.*, 2012, **112**, 5520-5551.
10. Y. Wei, X. Chang, T. Wang, C. Li and J. Gong, *Small*, 2017, **13**, 1702007.
11. L. Wang, J. Ge, A. Wang, M. Deng, X. Wang, S. Bai, R. Li, J. Jiang, Q. Zhang, Y. Luo and Y. Xiong, *Angew. Chem. Int. Ed.*, 2014, **53**, 5107-5111.
12. S. Ghose, S. Singh and T. S. Bhattacharya, *ACS Appl. Mater. Interfaces*, 2020, **12**, 7727-7735.
13. H. Feng, W. Wang, W. Wang, M. Zhang, C. Wang, C. Ma, W. Li and S. Chen, *J. Colloid Interface Sci.*, 2021, **601**, 531-543.
14. S. Wang, K. Teramura, T. Hisatomi, K. Domen, H. Asakura, S. Hosokawa and T. Tanaka, *Chem. Sci.*, 2021, **12**, 4940-4948.
15. L. Zhang, Z. J. Zhao and J. Gong, *Angew. Chem. Int. Ed.*, 2017, **56**, 11326-11353.
16. I. Platzman, R. Brener, H. Haick and R. Tannenbaum, *J. Phys. Chem. C*, 2008, **112**, 1101-1108.
17. C. Y. Toe, Z. Zheng, H. Wu, J. Scott, R. Amal and Y. H. Ng, *Angew. Chem. Int. Ed.*, 2018, **57**, 13613-13617.
18. C. Y. Toe, J. Scott, R. Amal and Y. H. Ng, *J. Photoch. Photobio. C*, 2019, **40**, 191-211.
19. L. Huang, R. Lu, W. Zhang, Y. Fan, Y. Du, K. Ni, Y. Zhu and M. Zhu, *Angew. Chem. Int. Ed.*, 2024, DOI: 10.1002/anie.202412964.
20. R. P. Mishra, M. Mrinalini, N. Kumar, S. Bastia and Y. S. Chaudhary, *Langmuir*, 2023, **39**, 14189-14203.
21. P. Preikschas, A. J. Martín, B. S. Yeo and J. Pérez-Ramírez, *Commun. Chem.*, 2023, **6**, 147.
22. H. Huo, H. He, C. Huang, X. Guan, F. Wu, Y. Du, H. Xing, E. Kan and A. Li, *Chem. Sci.*, 2024, **15**, 1638-1647.
23. J. Yin, X. Song, C. Sun, Y. Jiang, Y. He and H. Fei, *Angew. Chem. Int. Ed.*, 2024, **63**, e202316080.
24. H. Huo, T. Hu, C. Huang, F. Wu, T. Wang, X. Liu, L. Zhang, Q. Ju, Z. Zhong, H. Xing, E. Kan and A. Li, *J. Energy Chem.*, 2024, **93**, 202-212.
25. H. Shi, Y. Liang, J. Hou, H. Wang, Z. Jia, J. Wu, F. Song, H. Yang and X. Guo, *Angew. Chem. Int. Ed.*, 2024, **63**, e202404884.
26. X.-C. Xia, F. Cheng, P. Sun, A. A. Dubale, H. Han, E.-T. Cui, J. Song, X.-L. Yang and M.-H. Xie, *Chem. Eng. J.*, 2024, **491**, 152096.
27. M. Perfecto-Irigaray, I. Merino-Garcia, J. Albo, G. Beobide, O. Castillo, A. Luque and S. Pérez-Yáñez, *Mater. Today Energy*, 2023, **36**, 101346.
28. S. Gong, B. Ni, X. He, J. Wang, K. Jiang, D. Wu, Y. Min, H. Li and Z. Chen, *Energ. Environ. Sci.*, 2023, **16**, 5956-5969.
29. D. Montalvo, G. Corro, F. Bañuelos, O. Olivares-Xometl, P. Arellanes and U. Pal, *Appl. Catal. B*, 2023, **330**, 122652.
30. H. Shi, H. Wang, Y. Zhou, J. Li, P. Zhai, X. Li, G. G. Gurzadyan, J. Hou, H. Yang and X. Guo, *Angew. Chem. Int. Ed.*, 2022, **61**, e202208904.
31. H. Yu, C. Sun, Y. Xuan, K. Zhang and K. Chang, *Chem. Eng. J.*, 2022, **430**, 132940.
32. K. Das, R. Das, M. Riyaz, A. Parui, D. Bagchi, A. K. Singh, A. K. Singh, C. P. Vinod and S. C. Peter, *Adv. Mater.*, 2022, **35**, 2205994.
33. S. Bai, H. Qiu, M. Song, G. He, F. Wang, Y. Liu and L. Guo, *eScience*, 2022, **2**, 428-437.
34. D. Zhao, Y. Xuan, K. Zhang and X. Liu, *ChemSusChem*, 2021, **14**, 3293-3302.
35. G. Wang, C.-T. He, R. Huang, J. Mao, D. Wang and Y. Li, *J. Am. Chem. Soc.*, 2020, **142**, 19339-19345.